Astronomy & Astrophysics manuscript no. ms
April 12, 2024

ALMA-IMF XV: N_2H^+ kinematic analysis on the intermediate protocluster G353.41

R. H. Álvarez-Gutiérrez[1], A. M. Stutz[1], N. Sandoval-Garrido[1], F. Louvet[2], F. Motte[2], R. Galván-Madrid[3], N. Cunningham[2, 4], P. Sanhueza[5, 6], M. Bonfand[7], S. Bontemps[8], A. Gusdorf[9, 10], T. Csengeri[8], S. D. Reyes[1, 11], J. Salinas[1], T. Baug[12], L. Bronfman[13], G. Busquet[14, 15, 16], D. J. Díaz-González[3], M. Fernandez-Lopez[17], A. Guzmán[18], A. Koley[1], H.-L. Liu[19], F. A. Olguin[20], M. Valeille-Manet[8], F. Wyrowski[21]

(Affiliations can be found after the references)

Received XXX; accepted XXX

ABSTRACT

The ALMA-IMF Large Program provides multi-tracer observations of 15 Galactic massive protoclusters at matched sensitivity and spatial resolution. We focus on the dense gas kinematics of the G353.41 protocluster traced by N_2H^+ (1−0), with a critical density of 2×10^5 cm^{-3}, and spatial resolution ~ 0.02 pc. G353.41, at a distance of ~ 2 kpc, is embedded in a larger scale ($\sim$ 8 pc) filament and has a mass of $\sim 2.5 \times 10^3$ M$_\odot$ within 1.3×1.3 pc^2. We extract the N_2H^+ (1−0) isolated line component and we decompose it by fitting up to 3 Gaussian velocity components. This allows us to identify velocity structures that are either muddled or impossible to identify in the traditional position-velocity diagram. We identify multiple velocity gradients on large ($\sim$ 1 pc) and small scales ($\sim$0.2 pc). We find good agreement between the N_2H^+ velocities and the previously reported DCN core velocities, suggesting that cores are kinematically coupled to the dense gas in which they form. We measure 9 converging “V-shaped” velocity gradients ($\sim$ 20 km s^{-1} pc^{-1}) that are well-resolved (sizes $\sim$ 0.1 pc), located in filaments, and are sometimes associated with cores near their point of convergence. The average timescales associated with the V-shapes are $\sim$ 67 kyr, or about twice the free-fall time of cores in the same area ($\sim$ 33 kyr) but substantially shorter than protostar lifetime estimates ($\sim$ 0.5 Myr). We interpret these V-shapes as inflowing gas feeding the regions near cores (the immediate sites of star formation). We derive mass accretion rates in the range of $(0.35 - 8.77) \times 10^{-4}$ M$_\odot$ yr^{-1}. This feeding might lead to further filament collapse and formation of new cores. We suggest that the protocluster is collapsing on large scales, but the velocity signature of collapse is slow compared to pure free-fall. Thus these data are consistent with a comparatively slow global protocluster contraction under gravity, and faster core formation within, suggesting the formation of multiple generations of stars over the protocluster lifetime.

Key words. stars: formation – ISM: clouds – ISM: kinematics and dynamics – ISM: molecules

arXiv:2404.07363v1 [astro-ph.GA] 10 Apr 2024

1. Introduction

While star clusters have been studied extensively over many decades at comparatively short wavelengths, their precursors, protoclusters have not been studied in depth until recently. Protoclusters (or embedded clusters) are the gas-dominated maternal environments where star clusters are born and whose stellar constituents will ultimately populate the field of our Galaxy. Protoclusters are distinct entities from star clusters. Both are defined as relatively compact configurations where the gravity is strong enough to influence the dynamics of their constituents. But in the latter, there is little to no gas, and the gravity of the cluster is dominated by the stars themselves. In protoclusters, in contrast, gravity is dominated by the cold gas in which the stars themselves are forming (Stutz & Gould 2016; Csengeri et al. 2017; Stutz 2018; Motte et al. 2018). Protoclusters are more accessible now than ever before thanks to ALMA and its exquisitely high resolution interferometric mm-wave data tracing the cold gas where the stars form (Sanhueza et al. 2019; Liu et al. 2020a; Motte et al. 2022). Inside protoclusters we witness the ongoing conversion of gas into compact and extremely dense stars, a process mediated by gas filaments (Stutz 2018; González Lobos & Stutz 2019; Álvarez-Gutiérrez et al. 2021) feeding gas structures called “cores” (André et al. 2010; Stutz & Kainulainen 2015; Kuznetsova et al. 2015, 2018). Cores are compact gas mass concentrations, often defined to be of a size matching the resolution limit of the observations. In this case, we define cores to be order $\sim$ 2 kau, for reasons described below.

In this paper, we focus on the G353.41 protocluster (see Fig. 1), and in particular, on the dense gas kinematics observationally accessible from the protocluster scale (2.9 pc^2) to the core scale. We trace this dense and cold gas using the N_2H^+ (1-0) line observed with ALMA. Here N_2H^+, given its comparatively high critical density (see below), accesses the inner dense gas "skeleton" of the protocluster structure, free from confusion induced by lower density gas. Meanwhile, ALMA permits us to obtain the resolution needed to trace structures down to the core scales where individual or small numbers of stars may be forming.

The ALMA-IMF Large Program[1] (LP) maps 15 dense, nearby (2 − 5.5 kpc), and massive (2 − 32 $\times$ 10^3 M$_\odot$) Milky Way protoclusters down to ~2 kau scales (Motte et al. 2022), at matched spatial resolution. ALMA-IMF provides a large protocluster sample in order to test the universality of the stellar initial mass function (IMF) (Bastian et al. 2010; Offner et al. 2014). The ALMA-IMF LP also provides a vast catalogue of molecular lines, in bands 3 (2.6 − 3.6 mm) and 6 (1.1 − 1.4 mm). This rich molecular treasure trove allows for a detailed kinematical characterization of the gas, protostellar cores, and young stellar objects (YSOs) present in these protoclusters. The current

---

[1] Proposal ID 2017.1.01355.L, PIs: Motte, Ginsburg, Louvet, Sanhueza

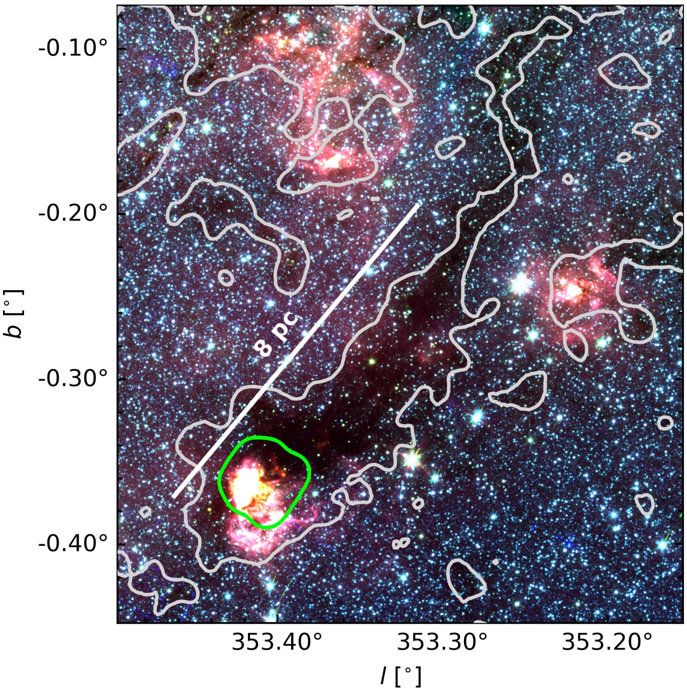

Fig. 1: Composite image of G353: IRAC 3.6 μm (in blue), 4.5 μm (green), and 5.8 μm (red). We indicate the ALMA-IMF N_2H^+ (1−0) coverage with a light green contour. We highlight ATLASGAL emission (870 μm) at 40 mJy beam^{-1} with the gray contour, corresponding roughly to a *Herschel* derived $N(H)$ of $\sim$ 5.5 10^{22} cm^{-2}.

publicly available ALMA-IMF data include, but are not limited to, continuum maps (Ginsburg et al. 2022; Díaz-González et al. 2023), 12 m data cubes of all spectral windows (Cunningham et al. 2023), core catalogues (Pouteau et al. 2022, Louvet et al. submitted), and hot core and outflow catalogues (Cunningham et al. 2023; Nony et al. 2023; Towner et al. 2024; Armante et al. 2024; Bonfand et al. 2024, Valeille-Manet et al. in prep). The data products derived from the ALMA-IMF LP allow us to constrain the different star forming environments, where we can analyze column densities, temperatures, outflow masses, core properties, and multi-tracer gas kinematics. This approach offers a thorough characterization of the processes taking place in these regions.

Motte et al. (2022) present a method of classifying these 15 protoclusters based on their evolutionary stage, assuming that they exhibit more H II regions as they evolve. They take into account the flux ratio between the 1 mm to 3 mm continuum maps ($S^{\rm cloud}_{1.3\,\rm mm}/S^{\rm cloud}_{3\,\rm mm}$), and the free-free emission at the frequency of H41α ($\sum^{\rm free-free}_{\rm H41\alpha}$). They find that as protoclusters evolve, $S^{\rm cloud}_{1.3\,\rm mm}/S^{\rm cloud}_{3\,\rm mm}$ decreases, while $\sum^{\rm free-free}_{\rm H41\alpha}$ increases (Motte et al. 2022, see their Fig. 3). Using these constraints, they group their 15 protocluster as being in a young, intermediate, or evolved evolutionary state. Out of these 15 regions, we analyze the G353.41 protocluster (hereafter G353). In Fig. 1 we indicate the ALMA-IMF N_2H^+ (1−0) coverage of G353 (centered at α,δ (J2000) = 17:30:26.28,−34:41:49.7) and its parent filament (dark lane traced by ATLASGAL 870 μm emission; Schuller et al. 2009) with light green and gray contours respectively. Motte et al. (2022) classify this protocluster as being at an intermediate evolutionary state, located at ∼2 kpc, and hosting a total mass of 2.5×10^3 M$_\odot$. They describe G353 as isolated, without obvious interaction with massive nearby stellar clusters. Using moment maps derived from the N_2H^+ (1−0) 12 m dataset they suggest the presence of multiple velocity components indicating a complex velocity field. They propose that G353 is composed of filaments interacting at the central hub. As presented in Bonfand et al. (2024), this region is an outlier in the ALMA-IMF hot core sample. Only one weak, low-mass (< 2 M$_\odot$) compact methyl formate source is detected and it lacks strong emission from complex organic molecules. They state that this protocluster is in a chemically poor stage, where further characterization of this region is required.

The N_2H^+ (1−0) transition (ν = 93.173809 GHz), given its high critical density, $n_{crit} = 2 \times 10^5$ cm^{-3} (Ungerechts et al. 1997), allows us to access the dense gas kinematics present in the innermost parts of star forming regions (Caselli et al. 2002a; Bergin et al. 2002; Tafalla et al. 2004; Lippok et al. 2013; Storm et al. 2014; Hacar et al. 2018; Chen et al. 2019; González Lobos & Stutz 2019; Álvarez-Gutiérrez et al. 2021). The J = 1→0 transition presents seven hyperfine components (Cazzoli et al. 1985; Caselli et al. 1995, 2002a). The kinematic analysis of this complex emission can be simplified by considering only the well separated isolated component (93.17631 GHz; $F_1, F = 0,1 \rightarrow 1,2$; Cazzoli et al. 1985). Such simplification is convenient to study the complex velocity fields found at the center of filaments. These regions present the densest environments for star formation, usually presenting multiple, blended velocity components, where the velocity distributions exhibit twists, turns, spirals, and wave-like patterns (Csengeri et al. 2011; Fernández-López et al. 2014; Stutz & Gould 2016; Liu et al. 2019; González Lobos & Stutz 2019; Álvarez-Gutiérrez et al. 2021; Sanhueza et al. 2021; Redaelli et al. 2022; Olguin et al. 2023). Recent techniques, such as the intensity-weighted position-velocity (PV) diagrams (González Lobos & Stutz 2019; Álvarez-Gutiérrez et al. 2021), allow us to characterize processes such as infall, outflow, or rotation present in these environments, where high spatial and spectral resolution studies open a window into the small scale gas kinematics of star forming regions. In addition to the PV diagrams, we can create Position-Position-Velocity (PPV) diagrams, in order to identify coherent structures that might be both spatially and kinematically associated (Chen et al. 2019; Henshaw et al. 2019; Sanhueza et al. 2021; Redaelli et al. 2022).

In this paper we investigate the N_2H^+ dense gas kinematics of G353 from large (protocluster) to small (cores) scales. In § 2 we present the data. In § 3 we introduce our N_2H^+ isolated extraction procedure. In § 4 we model and decompose the multiple velocity components found in the N_2H^+ isolated component spectra. In § 5 we show our gas kinematic analysis, from protocluster to core scales. In § 6 we show that G353 might be under gravitational collapse at small and large scales. In § 7 we estimate mass accretion rates for multiple velocity gradients characterized in our N_2H^+ data. We discuss our results in § 8, and we present our summary and conclusions in § 9.

2. Data

2.1. ALMA-IMF data

We make use of the N_2H^+ (1−0) 12 m, 7 m, and Total Power observations described in Motte et al. (2022) for our analysis, providing robust uv plane coverage. We image the combination of the N_2H^+ 7 m and 12 m (from now on called "7m+12m") measurement set of G353, using the publicly available imag-

Table 1: Relevant parameters of the N_2H^+ 7m+12m imaging

Field size	Pixel scale	Beam size	BPA [°]	^{a}RMS [K]	Channel width [km s^{-1}]	RMS velocity range [km s^{-1}]	^{b}V$_{\rm LSR}$ [km s^{-1}]
176″×172″ 1.72 pc×1.67 pc	0.72″ 1.44 kau	1.96″×2.29″ ~4 kau×4.6 kau	80.19	0.37	0.23	[−43 ; −32], [0 ; +7]	−17

Notes. ^{a} RMS value at the peak of the RMS distribution. ^{b} Obtained from Motte et al. (2022).

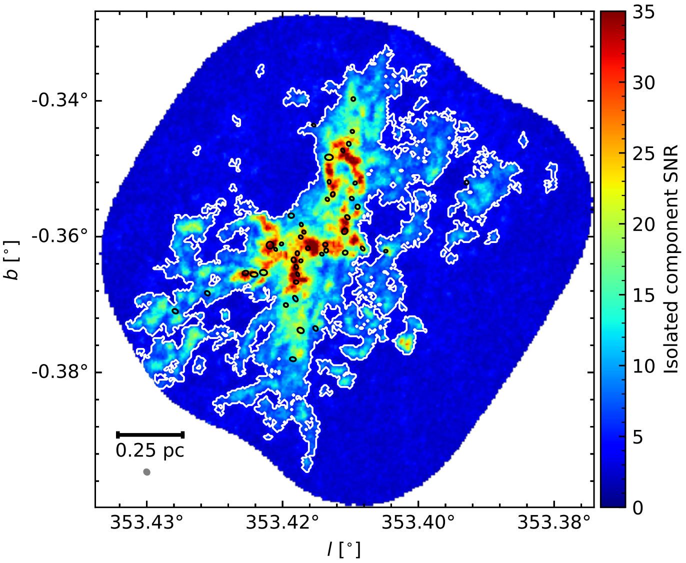

Fig. 2: G353 N_2H^+ isolated component SNR map. The white contour indicates the location of data with an isolated component SNR ≥ 5. We show the location of the 1.3 mm cores presented in Louvet et al. (submitted) with black ellipses and are located in regions with SNR ≥ 15. We indicate the beam size of these data with a gray ellipse at the bottom left corner. Outside the SNR contour we make a rough extraction of the isolated component (see text). For data inside the SNR contours, we implement a procedure based on detection of peaks and valleys, to individually extract high (≥ 5) SNR isolated components (see § 3).

ing scripts from the ALMA-IMF github repository[2]. These data are corrected by the primary beam response pattern. Due to the missing large-scale emission, we find that near the V$_{\rm LSR}$ of the protocluster (−17 km s^{-1}; Wienen et al. 2015; Motte et al. 2022) some subregions in the 7m+12m cube present deep negative artifacts ("negative bowls"). To cover all possible uv scales, we combine the N_2H^+ 7m+12m continuum-subtracted cube with the Total Power observations from the ALMA-IMF LP. We use the `feather`[3] task from `CASA 5.6.0`. With this combination, we were able to recover the missing flux, seen as negative bowls, present in the interferometric-only data. We produce a fully combined, multi-scale, feathered dataset which we use for our dense gas kinematic analysis.

To estimate and subtract the continuum emission present in the 7m+12m cube, we use the `imcontsub`[4] CASA task. We select the emission-free channels between −43 km s^{-1} and −33 km s^{-1}, and set the polynomial degree of the continuum fit (`fitorder`) to 0. We list relevant final image parameters in Table 1, such as the field size, pixel scale, beam size, root-mean-square noise (RMS), and channel width.

We use 12 m datacubes from Cunningham et al. (2023) to compare the shock tracers SiO (5 − 4) and CO (2 − 1) to our N_2H^+ kinematic analysis. We use DCN and N_2H^+ data to determine core velocities (§ 4.1). To determine total masses in specific regions we use the $N(H_2)$ map from Díaz-González et al. (2023).

2.2. Core properties from published catalogues

We use the 1.3 mm continuum derived cores catalogue[5], extracted using the `getsf` algorithm on the 1.3 mm continuum maps, smoothed at a common resolution of ~2700 au (45 sources, Louvet et al. submitted). We also use the DCN core velocities (15 sources, Cunningham et al. 2023) and the SiO outflow catalogue (16 sources, Towner et al. 2024) in order to look for correlation between the N_2H^+ gas kinematics and cores/outflows position and properties. It is worth mentioning that, within a radius of 0.3 pc from the center of G353 (Motte et al. 2022), we find 60% of the 1.3 mm cores (27 sources), and ∼ 70% of the cores with DCN velocities and SiO outflows (11 sources from each catalogue). Of these 11 outflows, 7 are "red" 3 are "blue" (monopolar), and 1 is "bipolar" (Towner et al. 2024). The presence of these sources might imply a complex velocity field in this region, given that cores and outflows disturb the kinematics of the surrounding gas.

3. N_2H^+ isolated component extraction

The N_2H^+ (1–0) transition is characterized by its hyperfine emission composed by seven components (Caselli et al. 1995, see their Fig. 1). We present an ideal example of N_2H^+ emission in Fig. 3, panel d. In this work we refer to the triplet of hyperfine components that present the highest intensities as the main N_2H^+ components, located at the center of the line emission at ν_{rest} = 93.173806 GHz. We refer to the most blueshifted hyperfine component as the isolated component, at ν_{rest} = 93.17631 GHz, shifted by ∼ −8 km s^{-1} relative to the main N_2H^+ component (see Table 1 from Cazzoli et al. 1985). We developed an algorithm to extract only the isolated hyperfine component from every pixel in the feathered datacube. This is in order to reduce the complexity of our data, given that it may contain multiple velocity components in addition to the hyperfine line emission. Considering that the N_2H^+ emission moves in velocity across the protocluster, our approach is to find the velocity where the emission of the isolated component ends and remove the rest of the line emission. We also preserve the emission-free channels, at low (−43 km s^{-1} to −31.5 km s^{-1}) and high (0.7 km s^{-1} to 6.7 km s^{-1}) velocities, to improve future RMS estimations if needed. Note that in the procedures de-

---

[2] https://github.com/ALMA-IMF/reduction

[3] https://casa.nrao.edu/docs/taskref/feather-task.html

[4] https://casa.nrao.edu/docs/taskref/imcontsub-task.html

[5] Available at www.almaimf.com

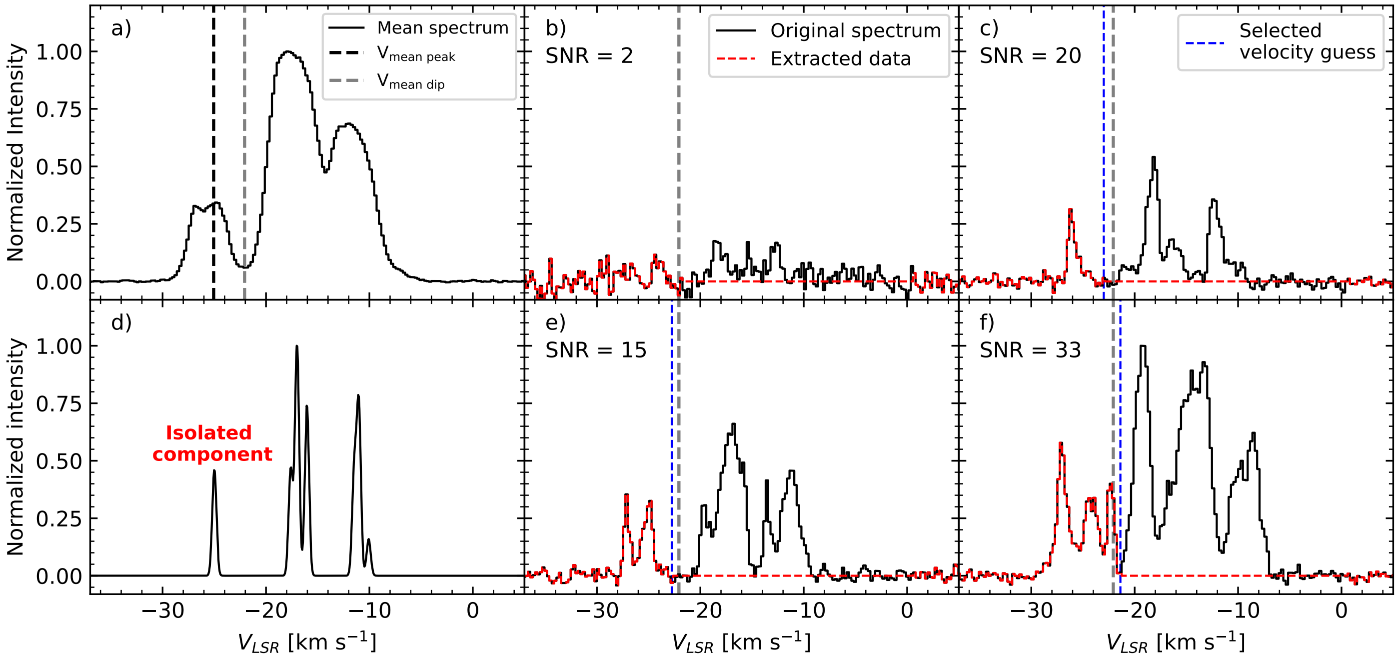

Fig. 3: **Panel a):** Normalized average N_2H^+ spectrum (solid black line) over the entire region. We show the location of the mean peak of the isolated component (dashed black line) and the "mean dip" (dashed gray line), see text. **Middle and right panels:** Normalized example spectra (within a pixel) of the N_2H^+ isolated velocity component extraction procedure (see § 3). We show G353 N_2H^+ spectra with solid black lines and the extracted isolated component, along with emission free channels, with dashed red lines. **Panel d):** Expected N_2H^+ emission for an excitation temperature of 15 K, an opacity of 1, velocity centroid of -17 km s^{-1}, and a line width of 0.2 km s^{-1}. We see the seven hyperfine components characteristic of this tracer, where the most blueshifted corresponds to the isolated component. To derive this emission we use "n2hp_vtau" model from `PySpecKit`. In panels b), c), e), and f) we indicate $V_{mean\ dip}$ with a dashed gray line. We present data with SNR < 5 in panel b), where we make a rough extraction based on the $V_{mean\ dip}$. We show data with SNR ≥ 5 in panels c), e), and f), presenting clear single, double, and triple N_2H^+ isolated velocity components respectively. In these examples we represent the selected velocity guess that separates the isolated component emission from the main line emission with dashed blue lines. The offset positions (Δl, Δb) of the spectra in panels b), c), e), and f) are (0.68 pc, 0.27 pc), (0.12 pc, -0.28 pc), (-0.08 pc, 0.47 pc), (0.16 pc, -0.07 pc) respectively. These offsets are estimated relative to the center of the region (See § 1).

scribed below, we use `find_peaks`[6] to detect peaks and valleys in different spectra.

Our extraction approach is separated into two procedures, for low and for high signal-to-noise (SNR) data. In order to determine which data have low or high SNR, we obtain the mean spectrum over all the spatial pixels of the cube, which serves as a guide to determine the velocity at the "mean dip" ($V_{mean\ dip}$ = -22 km s^{-1}, dashed gray line in Fig. 3 panel "a"). This velocity represents the mean location of the intensity valley between the isolated and the main components of the N_2H^+ emission. We define ΔV_{mean} = 3.2 km s^{-1} as the difference between $V_{mean\ dip}$ and the velocity at the peak of the mean isolated component $V_{mean\ peak}$ (dashed black line in Fig. 3 panel "a"), used in our velocity guesses for the high SNR extraction procedure (see below).

To create a SNR map of the isolated component, we first measure the RMS noise in emission-free channels (-43 km s^{-1} to -31.5 km s^{-1}), and the peak intensity in the channels range where the mean isolated component is located ($-$ 43 km s^{-1} to $V_{mean\ dip}$). This approach allows us to exclude the emission of the main line components. We encountered spurious emission at the edges of the SNR map. We adopt the procedure from Towner et al. (2024) by using the image processing techniques implemented by `binary_erosion`[7] (1 iteration) and `binary_propagation`[8] to clean the data for further analysis. `binary_erosion` allows us to remove the spurious emission in the outskirt of the map, although this approach also removes high SNR edges of our protocluster. Then, we use `binary_propagation` on the cleaned SNR map, using the original SNR map mask, to restore only the protocluster edges. To test our cleaning approach we compute the total integrated intensity using the Python package `SpectralCube`[9] in the range of -31.5 km s^{-1} to $V_{mean\ dip}$ using the original and cleaned SNR mask. We estimate that the removed spurious emission accounts for ~2% of the total integrated intensity for data with SNR> 5.

In Fig. 2 we show the N_2H^+ isolated component SNR map, where at SNR values ≥ 5 we capture the cloud emission while excluding noise (white contour). We set our isolated component SNR threshold to 5, in order to use one of the two extraction procedures (see below). In this section we refer to high (low) SNR spectrum if its isolated component SNR ≥ 5 (< 5). For low SNR spectra, we extract all the channels in the velocity range from $-$ 43 km s^{-1} up until $V_{mean\ dip}$ (panel "b" in Fig. 3). For high SNR spectra the extraction procedure consists of creating

---

[6] https://docs.scipy.org/doc/scipy/reference/generated/scipy.signal.find_peaks.html

[7] https://docs.scipy.org/doc/scipy/reference/generated/scipy.ndimage.binary_erosion.html

[8] https://docs.scipy.org/doc/scipy/reference/generated/scipy.ndimage.binary_propagation.html

[9] https://github.com/radio-astro-tools/spectral-cube

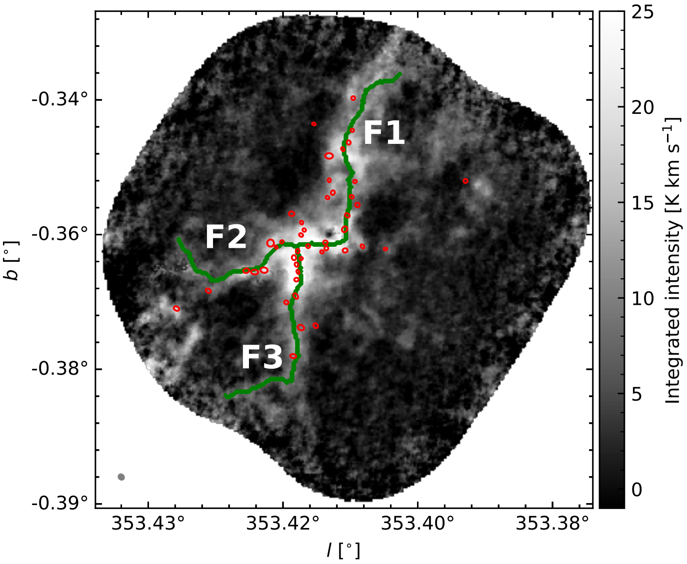

Fig. 4: Moment 0 map of the extracted N_2H^+ isolated component emission. We use the `FilFinder` Python package to identify the main filamentary structure present in G353 (see Appendix A). We identify three filaments (F1, F2, and F3; green lines) converging towards the central hub. The location of most of the 1.3 mm cores (red ellipses), projected in the POS, lie on top of the spine of these filaments, specially in the hub.

different velocity guesses that represent the location of the intensity valley, similar to the definition of $V_{mean\ dip}$ (Fig. 3). Then, we select a velocity guess based on its associated weight (see description below). This approach is described in detail here:

- First, we implement a rolling average along each spectra. This is in order to smooth over intensity bumps that might result in false positives for the detection of peaks and valleys. For this procedure, we average considering two channels before and after each velocity.
- After smoothing, for each spectra we identify the isolated component peak using `find_peaks`. We call the velocity associated to this peak $V_{isolated\ component}$. In the case of multiple velocity components it represents the most blueshifted one. We find the intensity valley between the isolated component and the N_2H^+ main line emission by inverting the spectra and finding the first peak which is the inverted intensity valley. We define the associated velocity to this intensity valley as $V_{first\ minima}$.
- We create three velocity guesses based on the properties of each spectrum in our cube (see points below). These are the 1^{st} guess: $V_{isolated\ component} + \Delta V_{mean}$. 2^{nd} guess: $V_{first\ minima}$. In the case of multiple isolated components this guess might incorrectly capture the intensity valley after the first isolated component. In that case, the other guesses are needed for a reliable isolated component extraction. 3^{rd} guess: $V_{mean\ dip} + \Delta V_{mean}$ to provide a velocity cut further away from the $V_{mean\ dip}$. This guess is mainly useful in the case where multiple isolated components cover a velocity range larger than the one probed by the other two guesses.
- From each velocity guess we estimate two parameters to later decide which one to use. One is the absolute value of its associated intensity "I_i" (i.e. intensity at the guess velocity), and the other is distance in velocity "dV_i" to the mean dip. The i subscript represents the guess associated to these parameters. We save the parameters of each guess in the lists "I" and "dV".
- We normalize these lists by their minimum value ensuring that the guess with the smallest "I_i" and "dV_i" will have a weight (w) of 1, defined in Eq 1. We do not encounter divergences in this normalization given these parameters are not exactly zero.

  $$w = (I_{norm} \times 0.2 + dV_{norm} \times 0.8)^{-1}, \tag{1}$$

  where the "norm" subscript indicates that the parameter list is divided by its minimum value.
- By visual inspection we consider that we obtain good extraction results when the weight is mostly dependent on dV and in a minor part on I. This is reflected by the 0.2 and 0.8 factors multiplying I_{norm} and dV_{norm} respectively, in the definition of "w" in Eq 1.
- We choose the guess with the weight closest to unity.
- Similarly as for SNR < 5, we extract the spectra from $-43\,\mathrm{km\,s^{-1}}$ up until the velocity of the chosen guess, and preserving the emission-free channels from $0.7\,\mathrm{km\,s^{-1}}$ to $6.7\,\mathrm{km\,s^{-1}}$.

Various examples of N_2H^+ spectra and isolated hyperfine component extraction are shown in Fig. 3, where we can see spectra containing one (panel "b"), two (panel "c"), and three (panel "d") velocity components, all well extracted by our procedure. In Stutz et al. (in prep) this approach is generalized to all ALMA-IMF regions for N_2H^+, providing reliable results. In Fig. 4 we show the moment 0 map estimated over the extracted N_2H^+ isolated velocity components. We use the `FilFinder` Python package (Koch & Rosolowsky 2015) in order to identify the most prominent filaments in this region (black lines in Fig. 4). We see that in the plane of the sky (POS) most of the 1.3 mm cores (red ellipses) are located on top of the filaments. This spatial agreement between filaments and protostelar cores is consistent with filamentary fragmentation (André et al. 2010; Busquet et al. 2013; Stutz & Kainulainen 2015; Kuznetsova et al. 2015, 2018). The procedure, including the parameters we used for the filamentary identification, is presented in Appendix A.

4. N_2H^+ isolated component velocity decomposition

In Fig. 3 we see that clear multiple isolated velocity components are present in our dataset. To characterize the complex dense-gas kinematics traced by N_2H^+ we follow the method in Álvarez-Gutiérrez et al. (2021), and we use the spectroscopic toolkit `PySpecKit` (Ginsburg & Mirocha 2011; Ginsburg et al. 2022) to model and decompose the isolated component emission. `PySpecKit` adjusts a fixed number of components set by the user, based on visual inspection of the data we impose three velocity components to every spectra and then remove false positives (see below). Given the kinematic complexity of the data and cursory inspection of the spectra, a simpler analysis with only two components contradicts the data. In essence, three components is the simplest possible choice, given the data. While this might fail for a small number of spectra that could require ≥ 4 velocity components, the residuals indicate that this could occur in a severe minority of cases, and hence more components is not warranted given the SNR and resolution of this particular data set. To improve the convergence of `PySpecKit`, we create a set of ranges for the parameters that define each of the three Gaussian velocity components, namely the peak intensity, central velocity, and velocity dispersion. After testing different parameter

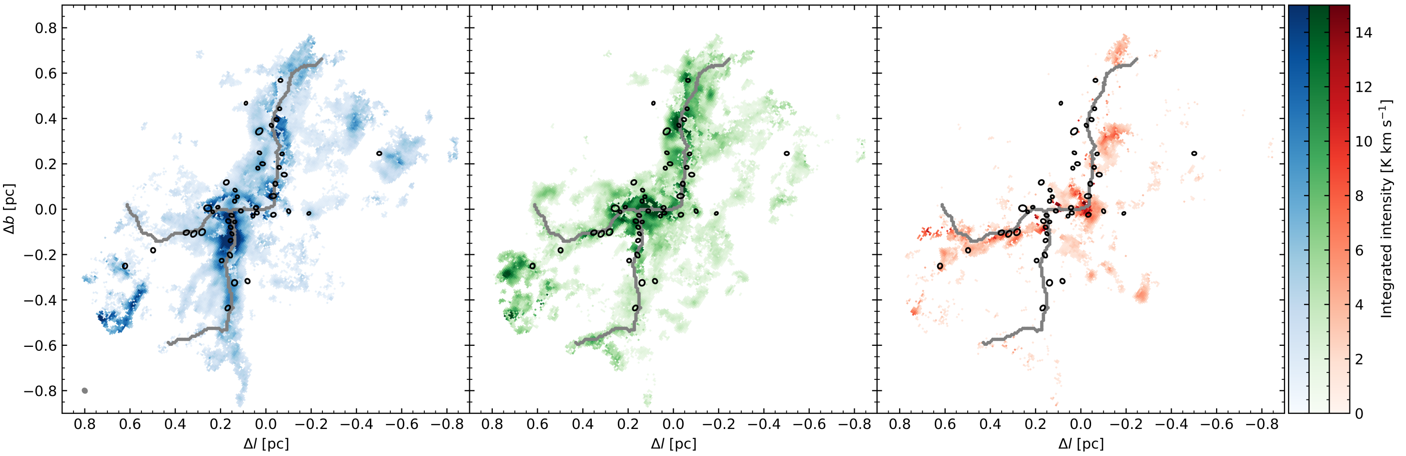

Fig. 5: Spatial distribution of the modeled Gaussian velocity components that describe the N_2H^+ isolated component emission. We indicate the main filament structure with green lines (see Fig. 4). In blue, green, and red we indicate the first, second, and third velocity components respectively. We indicate the beam size of these data with a gray ellipse at the bottom left corner. The emission of the first and second components is more extended and intense than the third, most red-shifted velocity component. The 1.3 mm cores match regions with high integrated intensity, mostly traced by the first and second velocity components.

ranges, we set the intensity range between 1.76 K (4 times the mean RMS) and 30 K, the velocity centroid from -30 km s^{-1} to -20 km s^{-1}, and the velocity dispersion from 0.22 km s^{-1} to 1 km s^{-1}.

From the results using the ranges defined above, we notice that some modeled components do not fit any emission. These fits are the result of imposing to the fitter a fixed number of components, given these spectra can be better represented by one or two velocity components. In these fits there is no uncertainty estimation for both the peak intensity and velocity dispersion. Based on these two criteria we remove those velocity fits from the modeled cube. With this cleaning approach we are left with spectra characterized by one ($\sim$ 34%), two ($\sim$ 53%), and three ($\sim$ 13%) Gaussian velocity components. We present the Gaussian fits of the high SNR spectra from Fig. 3 in Fig. B.1.

In Fig. 5 we show the spatial distribution of the multiple Gaussian velocity components. In gray we indicate the main filamentary structure in the region (see § 3). The first and second velocity components, in blue and green respectively, present most of the high intensity emission and they also spatially dominate over the third, most red-shifted component. Both the first and second components trace mostly the filaments F1 and F3 from Fig. 4, where most of the 1.3 mm cores are located. The position of these cores coincide with high integrated intensity regions in these isolated velocity components. The most redshifted component is compact and less intense compared to the first and second velocity components. This velocity distribution is located mostly along the filament F2 and the central hub (see Fig. 4). In Fig. 6 we present the number of Gaussian velocity components for each spectra, where we highlight that:

- Most of the N_2H^+ data presents emission characterized by two velocity components.
- Most of the spectra described by three velocity components are located in the innermost parts of the region.
- Most of the cores (black ellipses; Louvet et al. submitted) are located in regions with spectra presenting two to three Gaussian velocity components, indicating kinematic complexity even at ~4 kau (N_2H^+ spatial resolution).
- Single velocity component spectra are located preferentially in the outskirt of the protocluster.

In Fig. 7 we show the histogram of the fitted velocity centroid of each Gaussian velocity component. The peaks of these distributions are located at -27, -24.7, and -23.3 km s^{-1} respectively, well-separated in velocity. From hereafter we refer to these distribution as blue, green, and red respectively. Most of the velocity components appear to be associated with the blue and green distributions. For consistency with the different tracers used in further analysis, we shift the isolated component velocities by +8 km s^{-1}, to the reference frame of the main line components of N_2H^+ (Cazzoli et al. 1985).

4.1. DCN & N_2H^+ derived core velocities

In this section our goal is to increase the sample of core velocities from the already published DCN catalog, aiming to explore all the potential in these types of dataset. Given the relatively high n_{crit} of DCN (3–2) ($\sim$ 10^7 cm^{-3}) compared to N_2H^+ (1–0) (2×10^5 cm^{-3}), DCN (3–2) is known to coincide well with continuum peaks associated to cores (Liu et al. 2015; Cunningham et al. 2016; Minh et al. 2018), while N_2H^+ is characterized by tracing the dense gas at the innermost parts of star forming regions (Fernández-López et al. 2014; Hacar et al. 2018; González Lobos & Stutz 2019).

In Cunningham et al. (2023) they use ALMA-IMF 12 m observations of DCN (3−2) to study cores kinematics. They apply line emission fits for the DCN spectra inside the 1.3 mm cores from Louvet et al. (submitted). For this procedure they determine core velocities in all ALMA-IMF targets. They classify as DCN single and complex core velocities, spectra that can be fitted with one or multiple Gaussian velocity components respectively. Due to a global conservative SNR threshold the DCN fitting process missed the velocity estimation of some cores. For G353 only 15 out of the 45 cores present DCN velocity fits.

We use the ALMA-IMF DCN 12 m data from Cunningham et al. (2023), which presents a velocity resolution of $\sim$ 0.34 km s^{-1}. For each DCN velocity core described by a single component (Cunningham et al. 2023) we compare the emission of the DCN and modeled N_2H^+ isolated spectra. We find an average velocity offset between the DCN peak and the closest N_2H^+ isolated component peak of $\sim$ 0.65 km s^{-1}, less than two DCN

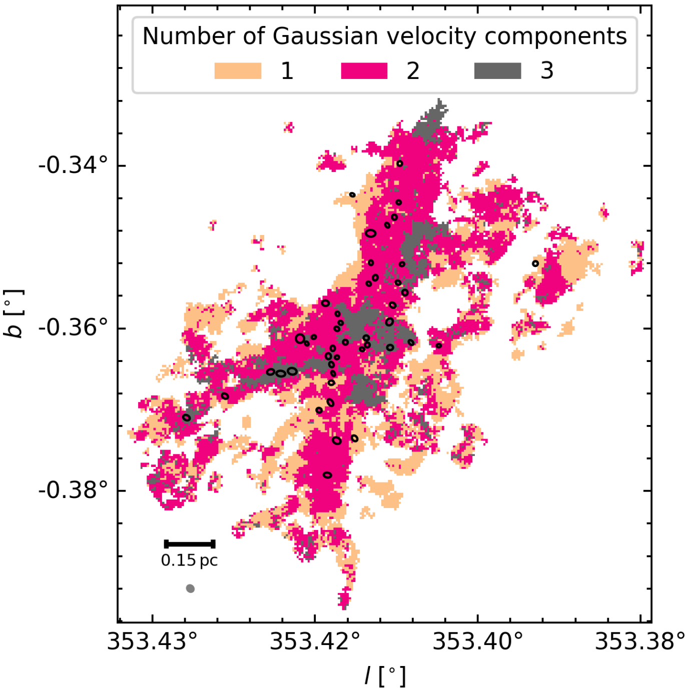

Fig. 6: Spatial distribution of the N_2H^+ spectra with up to three Gaussian velocity components. The 1.3 mm cores and beam size are the same as in Fig. 2. Most of the 1.3 mm cores are located in regions with spectra presenting two to three velocity components (see § 4).

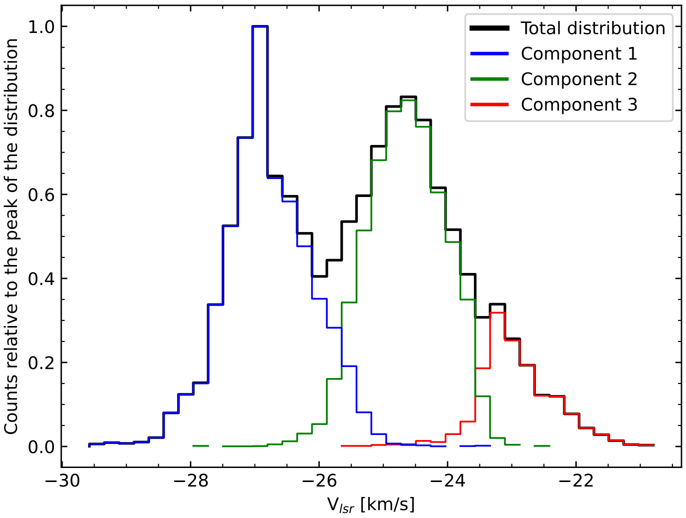

Fig. 7: Normalized velocity centroid distributions of each N_2H^+ Gaussian velocity component. The velocities at the peak of the distributions are – 26.9 km s^{-1}, – 24.7 km s^{-1}, and – 23.3 km s^{-1} for component 1 (blue), 2 (green), and 3 (red) respectively (see § 4).

channel widths. We use this approach for the remaining 30 cores, in order to determine their DCN velocities.

Here we estimate the RMS of the DCN data in emission-free channels in the range of -42 km s^{-1} to -25 km s^{-1} and we obtain the SNR map by dividing the peak intensity by the RMS. For the procedure below we only use DCN spectra with SNR > 3. Next, we extract the average DCN and modeled N_2H^+ isolated component spectra of these 30 cores. We identify the N_2H^+ isolated velocity component closest to the DCN peak within three DCN channel widths. We find that 11 out of these 30 cores present DCN with SNR $>$ 3 close to one N_2H^+ velocity component. Here, we define the velocity of these cores as the velocity where the DCN emission peaks. On average, these cores have a velocity offset between these two tracers less than 0.8 km s^{-1} ($<$ 2.5 DCN channels), similar to the results obtained for the 15 cores with DCN velocities from Cunningham et al. (2023), and they present an average velocity offset of 0.38 km s^{-1}. Throughout this paper we refer to these cores as "DCN & N_2H^+ cores" given they are derived from the comparison of these two tracers. In Table C.1 we include these DCN & N_2H^+ core velocities, complementing the DCN catalogue from Cunningham et al. (2023). In Fig. C.1 we present two examples of DCN and N_2H^+ spectra in cores where we see clear agreement between these tracers.

5. Analysis of position-velocity diagrams

5.1. Traditional PV diagram

We start by analyzing the "traditional" PV diagram shown in Fig. 8. We create this diagram by taking the total intensity along the Galactic longitude, where Δb indicates the distance in parsec relative to the center of G353, assuming a distance to the protocluster of of 2 kpc (Motte et al. 2022). We see general agreement between the DCN core velocities and the N_2H^+ velocity distribution. This suggests that most of the cores are still kinematically coupled to the dense gas in which they formed. As presented in § 4.1, the DCN and N_2H^+ velocities match within 0.8 km s^{-1} ($<$ 2.5 DCN channels).

Regarding the dense gas velocity distribution, in Fig. 8 we see a velocity spread of $\sim$ 8 km s^{-1} in the sub-region between $\Delta b \sim -0.3$ pc to 0.1 pc. Most of the intensity on this diagram is located at the upper part of this sub-region, at Δb ± 0.1 pc. This spread is also present in the PV diagram along Δb and Δl shown in the top right and bottom left panel of Fig. 9. We explore the possible origin of this structure in § 6.

5.2. Intensity-weighted PV diagrams

In the top left panel of Fig. 9 we show the spatial distribution of the fitted Gaussian velocity components (see § 4). The blue, green, and red color maps indicate the integrated intensity of the first, second, and third velocity components of the N_2H^+ spectra respectively. Note that the spatial overlap between any of these components is presented in Fig. 6.

As seen in Fig. 8, the traditional PV diagram provides information on the dynamics on the large, protocluster-scale, environment. Meanwhile, the intensity-weighted position-velocity diagram (Fig. 9), where the color of each point indicates its integrated intensity, highlights the small core-scale kinematics. Similarly as in González Lobos & Stutz (2019) and Álvarez-Gutiérrez et al. (2021), from the isolated component line decomposition (§ 4), we derive the integrated intensity and velocity centroid for each Gaussian velocity component. Using these parameters we create intensity-weighted PV diagrams along the b and l coordinates. We present these N_2H^+ PV diagrams in the bottom left and top right panels of Fig. 9. The key features on the position-position (PP) and on the top right PV diagram, are:

- The agreement between the DCN core velocities and the overall N_2H^+ PV structures suggests that cores are still kinematically coupled to the dense gas in which they formed.

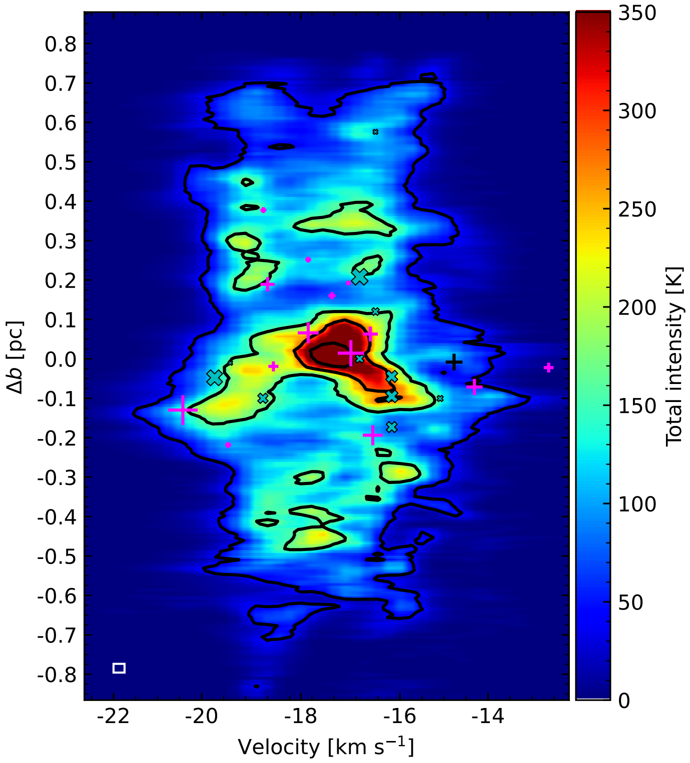

Fig. 8: "Traditional" PV diagram of the N_2H^+ modeled isolated components, created by collapsing the l coordinate. Δb indicates the distance along b in pc, relative to the center of G353, assuming a distance of 2 kpc (Motte et al. 2022). The colormap indicates the total intensity along l. With fuchsia and black crosses we show the 1.3 mm cores with single and complex DCN velocities detections, respectively (Cunningham et al. 2023). With dark cyan "×" markers we show the 1.3 mm cores with velocities derived from DCN and N_2H^+ data (see § 4.1). The size of the markers indicate relative mass (Louvet et al. submitted). Black contours indicate total intensities at 40, 160, 280, and 400 K. We see a large scale velocity spread ($\Delta V \sim 8$ km s^{-1}) around $\Delta b \sim -0.3$ pc $-$ 0.13 pc (see also § 5.2). We show the major axis of the beam and the channel width with a white rectangle at the bottom left corner.

- We see at least nine clear and prominent V-shaped velocity gradients (see Fig. D.1), across all velocity components. The orientation of these V-shape, pointing to the left/right (top right panel) or up/down (bottom left panel), follow no clear preference.
- In some cases, the vertex of these V-shapes is close spatially and in velocity to the location of cores.
- In the plane of the sky (POS), all three velocity components overlap in most of the region.
- This technique recovers the large scale velocity spread present in Fig. 8 and highlights small scale structures.
- The most prominent V-shape is located at (Δb, V) = (−0.14 pc, −20.5 km s^{-1}), between two 1.3 mm cores with DCN detections (see § 6).

For a better visualization of the 3D structure of these V-shapes we provide an interactive 3D PPV diagram at: `rodrigoalvarez.space/research/figures`.

5.3. Velocity gradients

In this section we focus on the most prominent blue V-shape (Fig. 9, top right panel). In Fig. 10 we show this velocity distribution in detail. In order to characterize the VGs composing this V-shape, we apply a linear fit to both the upper and lower VG. Given the visual linearity of the VGs composing the V-shape, we apply a linear fit to these distribution in order to characterize them. For these fits we consider data only above an integrated intensity threshold of 8 K km s^{-1} and 3 K km s^{-1}, for the upper and lower gradient respectively. We remove data not related to the velocity gradient, clustered in the ranges of (Δb, V) $\sim$ (−0.025 − 0.04 pc , −19.5 − −18.5 km s^{-1}), which lie just outside the filament hosting this V-shape on the POS. Additionally, we weight each point based on their integrated intensity to make our fits more robust. The slopes of the linear fits represent the VGs in km s^{-1} pc^{-1}. These linear fits follow the VGs distribution and these are somewhat asymmetric, the upper gradient is slightly shallower than the bottom gradient. Given the unknown inclination angle (θ) of these structures relative to the POS, the observed VG is just a fraction of the original VG. These are related as $\mathrm{VG} = \mathrm{VG}_{original} \cdot \sin(\theta)$. These VGs present values between ~ 13 to ~ 18 km s^{-1} pc^{-1} (see Fig. 10). Additionally, we estimate the center of this V-shape as the velocity-weighted mean position of the points composing this structure. With this approach the position of the points closest to the V-shape apex present more weight, obtaining the center of this V-shape at (l, b) = (353.4135°, −0.3657°). This position is located between "core 2" and "core 3", both of them having DCN velocity fits (Cunningham et al. 2023). These core present masses of 20.7 and 6.4 $M_\odot$ respectively. We inspect the core catalog derived from the map at native resolution (Louvet et al. submitted) and the location of this V-shape do not coincide with any core.

In the left panel of Fig. 11 we show the integrated intensity of the multiple modeled N_2H^+ isolated components. With colored boxes we show the areas where we create the different PV diagrams presented on the right panel. These boxes are centered at the main blue V-shape, matching the area of this V-shaped structure (see Fig. 12). We show that the overall structure in PV space is conserved at different angles, excluding the possibility of this velocity feature being the result of projection effects.

For this V-shaped structure, we note that the N_2H^+ velocity range is $\Delta V \sim 2$ km s^{-1}, while the whole N_2H^+ isolated component dataset present a $\Delta V \sim 8$ km s^{-1} (Fig. 9). From these VGs we derive timescales as $t_{VG} = 1/\mathrm{VG}$, similar to the procedure for a rotating filament presented in Álvarez-Gutiérrez et al. (2021). We obtain timescales between $\sim$ 50 − 70 kyr. These timescales are short compared to the $\sim$ 0.21 Myr free fall time (t_{ff}) of the protocluster (Motte et al. 2022), and a few times larger than the t_{ff} of nearby cores ($\sim$ 20 kyr, within 0.1 pc of this V-shape). To determine the cores t_{ff}, we use the 1.3 mm core masses from Louvet et al. (submitted). We characterized eight more N_2H^+ V-shaped structure. These are presented in Appendix D. Note that within a ~beam size from the apex of V-shape "B" (see Fig. D.2), the continuum core "7" ($\sim 6\,M_\odot$) is located.

In Henshaw et al. (2014), they propose two scenarios that might produce these V-shaped velocity gradients (see their Fig. 12). One scenario suggests that gas in a filament is flowing towards a denser region (infall), while the other scenario suggests that a protostellar outflow moves the dense gas located in its vicinity. To analyze the different dynamical processes present in this region, we use the ALMA-IMF 12 m data of the shock, outflow tracer SiO (5−4), from Cunningham et al. (2023). From

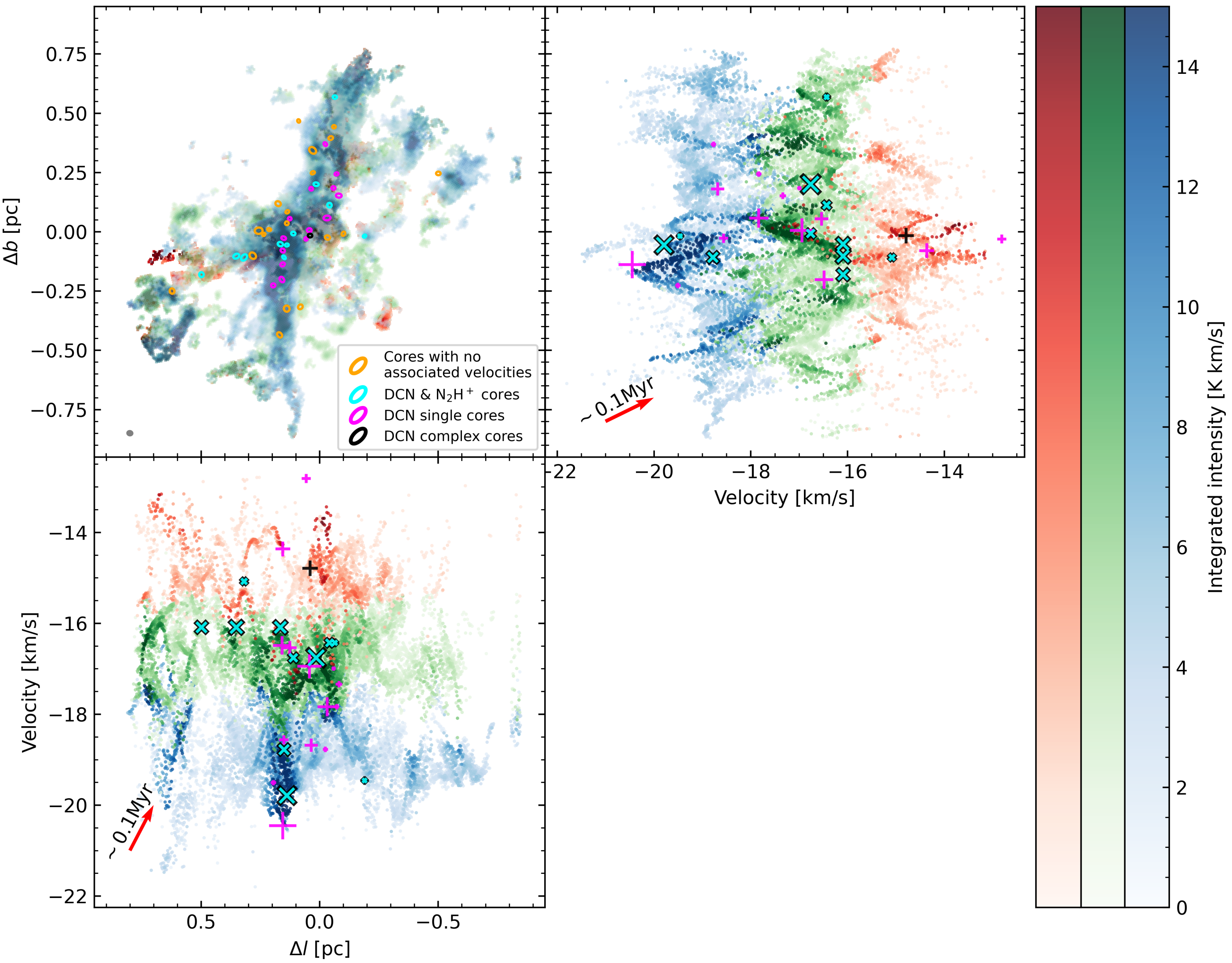

Fig. 9: **Top Left:** Spatial distribution of the fitted N_2H^+ Gaussian isolated velocity components (blue, green, and red, see § 4). Ellipses indicate the location of the 1.3 mm continuum cores (Louvet et al. submitted). Orange indicates cores with no DCN detections. Fuchsia and black represent cores with single and complex DCN velocities (Cunningham et al. 2023). DCN & N_2H^+ cores are indicated with cyan. We show the beam size with a gray ellipse in the bottom left corner. **Top right and bottom left:** Intensity-weighted position-velocity diagrams along the *b* and *l* coordinates respectively. For the 1.3 mm core velocities we use the same colors and markers convention from Fig. 8. For reference we indicate with a red arrow, in both the top right and bottom left panels, a velocity gradient of 10 $\mathrm{km\,s^{-1}\,pc^{-1}}$ corresponding to a timescale of ∼ 0.1 Myr. We see multiple V-shapes near the location of cores across all velocities in the PV diagrams, more prominently in the top right panel. The most prominent V-shape is located in the blue component, at $(\mathrm{V}, \Delta\mathrm{b}) \sim (-20.5\,\mathrm{km\,s^{-1}}, -0.14\,\mathrm{pc})$ (see § 5.2). We provide an interactive 3D PPV diagram at: `rodrigoalvarez.space/research/figures`.

those data we create its intensity-weighted PV diagram, presented in Fig. E.1 (see Appendix E for more details). We note that there is almost no SiO emission nor outflow sources at the location of the N_2H^+ V-shape (see Fig. 12). The ΔV within 10″ from this main blue V-shape is ∼40 $\mathrm{km\,s^{-1}}$, while for the whole SiO dataset is ∼80 $\mathrm{km\,s^{-1}}$, showing a clear difference in the SiO ΔV and the core velocities. Furthermore, the SiO ΔV is ∼ 10 times larger than the one of N_2H^+. This difference in traced velocities implies that these two molecules trace vastly different physical phenomena. We suggest that the small velocity range probed by N_2H^+ indicates that the velocity gradients can be considered as infall signatures (see § 6). We discuss the possible morphology of the filaments hosting V-shapes in § 8.

6. G353 as a collapsing region

We use the SiO (5 − 4) and CO (2 − 1) data from Towner et al. (2024) and Cunningham et al. (2023) to identify possible outflows near the V-shape presented in Fig. 10. For CO we measure the RMS in the emission-free velocity range of 145 to 286 $\mathrm{km\,s^{-1}}$. We use only CO data with SNR > 3 for our analysis. The cleaning of the SiO data is described in Appendix E. In Fig. 12, with a fuchsia "×" we indicate the center of the V-shape from § 5.3, located between two 1.3 mm cores 2 & 3 (black ellipses), which present DCN velocity detections. From these diagrams we see there is neither SiO nor CO outflow detection at the location of the main blue V-shape $(\Delta l, \Delta b) = (0\,\mathrm{pc}, 0\,\mathrm{pc})$. In the right panel we show the position

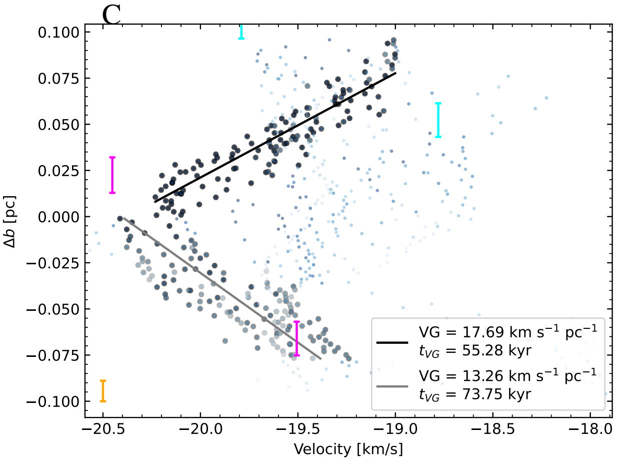

Fig. 10: Zoomed-in version of the top right panel of Fig. 9, centered at the prominent blue V-shape ("C") located at $(\Delta b, \mathrm{V}) = (-0.14\,\mathrm{pc}, \text{-}20.5\,\mathrm{km\,s^{-1}})$. We indicate the major axis of the cores with vertical lines in fuchsia (DCN single) and cyan (N_2H^+), similarly we represent the major axis of the beam with an orange vertical line. We apply linear fits to the upper and lower distributions, represented by darker points. These points are selected based on an integrated intensity threshold (see § 5.3). We weight each point by their integrated intensity and derive velocity gradients (VGs) from the slope of these linear fits. The range of the obtained VGs is $\sim 13 - 18\,\mathrm{km\,s^{-1}\,pc^{-1}}$. We define the timescales associated to the VG as $t_{VG} = \mathrm{VG}^{-1}$, being in the range of $\sim 50 - 70$ kyr. We show eight more well characterized V-shapes in Appendix D.

of the data composing this V-shape, where the velocity peaks towards the center of this velocity feature.

We derive the mass-weighted mean position of the two cores (2 & 3) closest to the V-shape to determine their barycenter (yellow "×" in Fig. 12). We find that the difference between the center of the V-shape and the barycenter of these cores is $\sim 0.3''(\sim 600\mathrm{au})$, well below the beam size of the N_2H^+ data. A similar offset is also present in the intensity and velocity profiles along filaments from ATOMS data (Zhou et al. 2022, see their Fig. 6). This small spatial offset might suggest that the gas flowing in the V-shape is produced by the gravitational pull towards the barycenter of cores 2 & 3, where the N_2H^+ radial velocities peak. This interpretation is similar to the one proposed in Zhou et al. (2023) in their kinematic analysis of the G333 complex. They describe the V-shaped velocity gradients as the result of gas funneling from the molecular cloud to clumps which is then funneled into cores (see their Fig. 9) consistent with gravitational acceleration.

In Fig. 13 we show the mean spectra of different tracers at the central position of the main blue V-shape. These spectra are measured over a circular region with diameter equal to the major axis of the N_2H^+ beam ($2.28''$; ~ 0.02 pc). This circular area results in a coverage of 1.14 times the N_2H^+ beam, and ~5.6 times the beams of the H_2CO, DCN, and $H_2{}^{13}CO$ data. We see N_2H^+ and H_2CO present double component spectra with asymmetric peaks. Between these peaks we detect DCN and $H_2{}^{13}CO$ emission. The asymmetric spectra present in N_2H^+ and H_2CO is consistent with the "blue asymmetry" spectral feature, usually interpreted as infall signature, suggesting that this region is under gravitational collapse (e.g. Anglada et al. 1987; Mardones et al. 1997; Lee et al. 1999, 2001; Smith et al. 2012). Based on the idea that the V-shapes are the result of flowing gas along filaments towards denser regions, the blue-asymmetry detected at the center of the main blue V-shape suggests that gravitational collapse is taking place at the apex of the V-shaped structure.

Regarding large scales, in the traditional PV diagram presented § 5.1 (see Fig. 8), we see a clear velocity spread around $\Delta\ b \sim -0.1$ pc, also present in the top right panel of Fig. 9. Below we compare this velocity spread with the velocity distribution produced by infall, where the gas velocities increase as the distance to the center of infall ("r") decreases:

$$V_{infall} = -\sqrt{\frac{2G\,M}{r}} \tag{2}$$

For this comparison we model a sphere with a total mass of 150 $M_\odot$, a radius of 0.5 pc, and a power law density profile described by:

$$\rho(r) = \rho_0 \left(\frac{r}{\mathrm{pc}}\right)^{-\gamma}, \ \gamma = 5.65, \ \rho_0 = 6.1 \times 10^{-5}\,\frac{\mathrm{M_\odot}}{\mathrm{pc}^3}, \tag{3}$$

we provide the derivation of $\rho(r)$ in Appendix F. $\gamma = 5.65$ was determined by visual inspection by comparing the obtained radial velocities of the model (see below), at different γ values, with the overall shape of the PV distribution.

We then estimate the infall velocity of each point, based on the cumulative mass distribution ("M") at any given distance to the center (Eq. 2). We obtain the radial component of the infalling velocities as:

$$V_r = V_{infall} \times \cos(\arctan(X/Z)), \tag{4}$$

where X represents the horizontal coordinate in the POS, while Z represents the (non-observed) depth of the sphere.

In Fig. 14, we show the coverage of the PV distribution from our model with a solid white line. We find good agreement between the PV distributions of our approach and the data. The PV distribution of our infall model is consistent with previous work that provide the expected PV distributions for spherical protostellar envelopes under infall (Tobin et al. 2012). At large scales we interpret the agreement between the PV diagrams of our model and the data as protocluster scale collapse due to gravitational contraction. It is worth noting that the mass of our model ~5.5 times lower than the mass derived from the $N(H_2)$ map (Díaz-González et al. 2023). We speculate that a model considering complex processes such as turbulence, radiative transfer, and magnetic fields might solve this mass discrepancy while still matching the observed PV distribution.

7. Mass accretion rates in the V-shaped structure

Based on the idea that the V-shapes are a result of gas flowing toward cores, in this section we provide estimates of their mass accretion rates ($\dot{M}_{\mathrm{in}}$) for N_2H^+ and H_2.

7.1. N_2H^+ mass accretion rate

To derive the $\dot{M}_{\mathrm{in}}$ associated to the main blue V-shape (Fig. 10), we need to estimate its N_2H^+ mass. For this procedure we use `PySpecKit` with the `n2hp_vtau` fitter, to fit the full N_2H^+ line. The fitted parameters (see below) allow us to derive the $N(N_2H^+)$. The V-shape structure contains 77, 143, and 25 N_2H^+

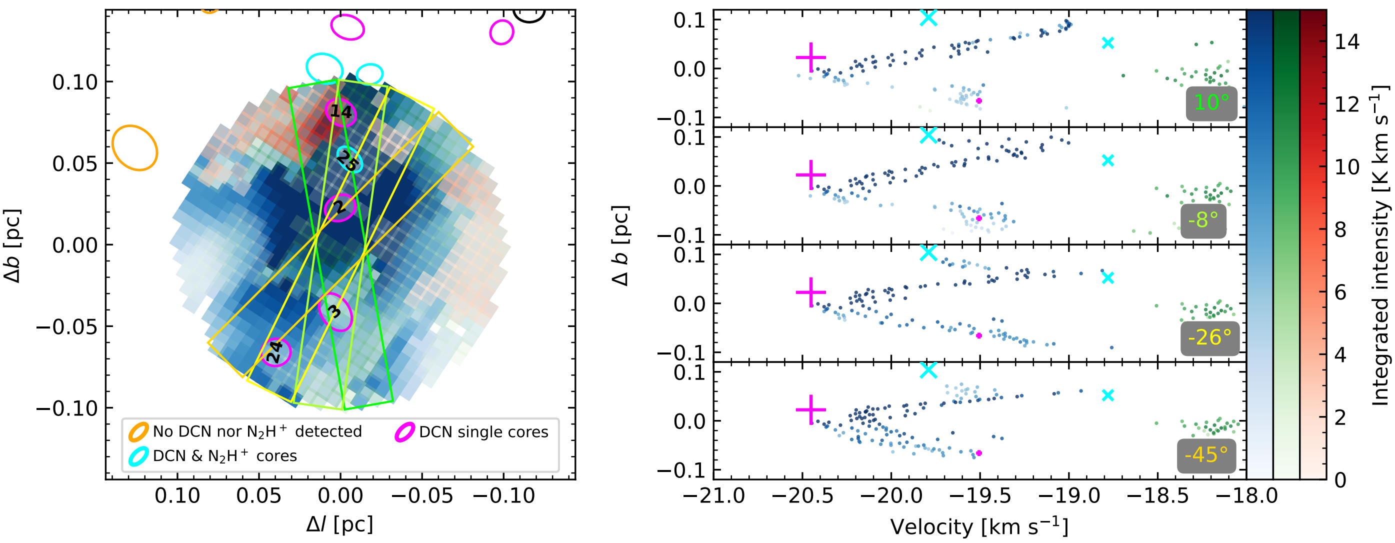

Fig. 11: **Left panel:** Integrated intensity map of the modeled N_2H^+ isolated component, inside a region centered at the main blue V-shape with a radius of 0.1 pc. With boxes in shades of green and yellow, we indicate the different paths taken to create the PV diagrams shown on the right panel. The area covered by these four PVs matches the extent of this V-shape (see Fig. 12). The 1.3 mm cores are indicated using the same convention from Fig. 9. For the cores within the radius of 0.1 pc we indicate their IDs in black. **Right panel:** PV diagrams corresponding to the different paths presented in the left panel. At the bottom right corner of each sub panel, with colored values, we indicate the angle (counter-clockwise) of each PV path. The PV paths match the V-shape coverage (right panel of Fig. 12). We see the overall structure of this V-shape persists at different angles, indicating that these structures are not a result of projection in the POS.

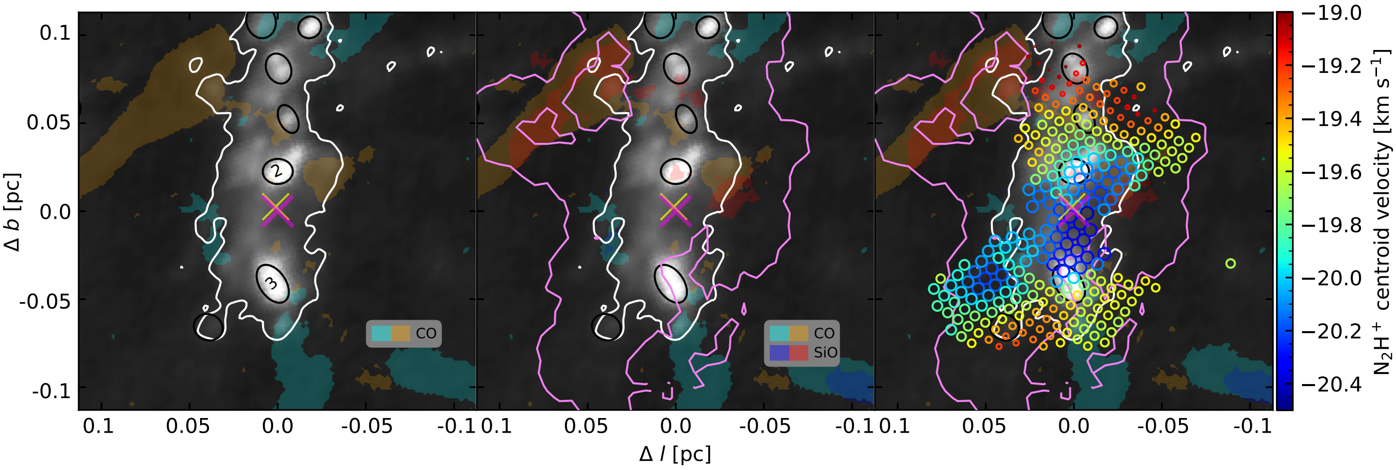

Fig. 12: Multi-tracer diagram at the location of the main blue V-shape of G353 (§ 5.3). The different panels show the step by step construction of the final plot (right panel). **Left panel:** The black to white background shows the 1.3 mm continuum emission from Díaz-González et al. (2023). With black ellipses we show the 1.3 mm continuum cores from Louvet et al. (submitted). With black text we indicate the IDs of the cores closest to the center of the V-shape, marked with a fuchsia "×". We indicate the barycenter of cores 2 & 3 (see Fig. 11) with a yellow "×". Filled contours represent the CO (2-1) emission in the velocity ranges of $-50\ \mathrm{km\,s^{-1}}$ to $-15\ \mathrm{km\,s^{-1}}$ (cyan) and $15\ \mathrm{km\,s^{-1}}$ to $50\ \mathrm{km\,s^{-1}}$ (beige), relative to the $V_{LSR} = -17\,\mathrm{km\,s^{-1}}$ of G353. With a white contour we indicate the $log(N(H_2)\ \mathrm{cm}^2) = 23.3$. **Middle panel:** In addition to the left panel, we include the SiO $(5-4)$ emission with blue and red contours in the same (negative and positive) velocity range as with CO. The pink contour indicates the integrated intensity of the most blueshifted modeled N_2H^+ Gaussian velocity component (see Fig. 9; blue distribution), at a value of $7\ \mathrm{K\ km\,s^{-1}}$. **Right panel:** With open circles we show the location of the data composing the main N_2H^+ blue V-shape. The colors indicate their velocity centroid, and their (increasing) size indicates how close the gas velocities are to the velocity apex of the V-shape. This velocity gradient seems to converge to the barycenter of cores 2 & 3, and it is oriented along a filament.

spectra with one, two, and three velocity components respectively. The bluest velocities in the three velocity component spectra accounts for ∼2% of the total number of velocities in this V-shape. For this reason, we model the full N_2H^+ hyperfine line structure with one and two velocity components. In Table 2 we list the parameters and ranges used for this procedure.

After obtaining the modeled N_2H^+ cube, we remove modeled components where $\tau_{\mathrm{RMS}}/\tau > 0.3$, where τ and τ_{RMS} represent the estimated opacity and its associated error, respectively.

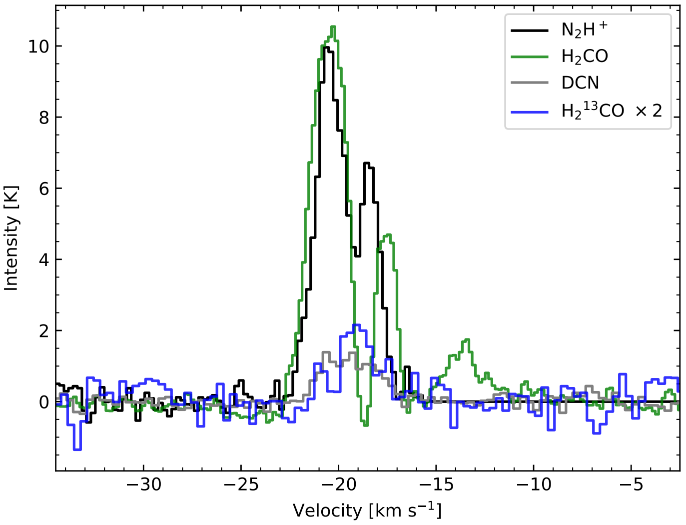

Fig. 13: Mean spectra within a 1.14″ (∼ 0.01 pc) radius around the location of the main blue V-shape (pink "×" in Fig. 12). Both N_2H^+ and H_2CO show blue asymmetry, known to characterize infall motions.

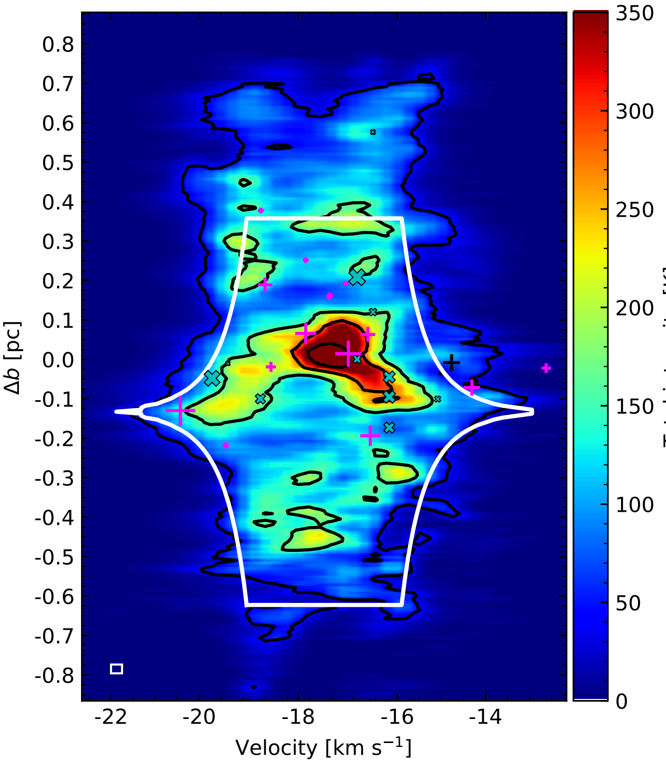

Fig. 14: PV coverage of a gravitationally collapsing sphere. The white contour represents the coverage of the synthetic radial velocities derived from this model (§ 6). The background and cores are the same as in Fig. 8. For the modeled sphere we set its total mass to 150 $M_\odot$, within a radius of 0.5 pc.

This criterion is to ensure that we use reliable fitted parameters to determine our $N(N_2H^+)$ values. For the fitting of two N_2H^+ components we only analyze the most blueshifted component. The resulting opacities follow a log-normal distribution with a peak at $\tau = 0.13$.

Table 2: N_2H^+ full line fitting parameter ranges

Excitation temperature [K]	(T_{ex})	2.73 – 80
Opacity	(τ)	0.01 – 40
Centroid velocity [km s^{-1}]	(v)	−25 – 15
Velocity dispersion [km s^{-1}]	(Δv)	0.20 – 3

Notes. Ranges used for the full N_2H^+ line fitting.

We derive the $N(N_2H^+)$ of the V-shape by using Eq. 5 (Caselli et al. 2002b):

$$N(N_2H^+) = \frac{8\pi^{3/2}\Delta v}{2\sqrt{\ln 2}\lambda^3 A}\frac{g_l}{g_u}\frac{\tau}{1-\exp\left(-h\nu/k\mathrm{T_{ex}}\right)}\frac{Q_{\rm rot}}{g_l\exp(-E_l/k\mathrm{T_{ex}})}, \tag{5}$$

Where τ, T_{ex}, and Δv are the opacity, excitation temperature, and velocity dispersion respectively, obtained from the full line fitting. The Planck and Boltzmann constants are represented by h and k respectively, ν and λ are the frequency and wavelength of N_2H^+, A is the Einstein coefficient of the N_2H^+ (1−0) transition, g_l and g_u are the statistical weights of the lower and upper energy levels, $Q_{\rm rot}$ is the partition function, and E_l is the energy of the lower level.

From the above procedure, inside the V-shaped structure, we get a total $N(N_2H^+) = 5.24 \times 10^{15}$ cm^{-2} and a total $M(N_2H^+) = 5.9 \times 10^{-8}$ $M_\odot$. We use the average timescale of the VGs from § 5.3 (Fig. 10), $t_{VG\ mean}$ = 64.5 kyr, to determine the $\dot{M}_{\rm in}$ (N_2H^+) as:

$$\dot{M}_{\rm in}(N_2H^+) = \frac{M(N_2H^+)}{t_{VG\ mean}} = 9.1 \times 10^{-13}\ M_\odot\,{\rm yr}^{-1}. \tag{6}$$

Note that the $\dot{M}_{\rm in}(N_2H^+)$ estimate (and $\dot{M}_{\rm in}(H_2)$ below) should be multiplied by $\sin(\theta)$, in order to account for the unknown inclination angle (θ) of the protocluster/filaments relative to the POS.

7.2. H_2 mass accretion rate

To ensure that we estimate the V-shape $M(H_2)$ on the same area as in the N_2H^+ hyperfine line fitting, we use the CASA task `imregrid` to obtain the continuum-derived $N(H_2)$ map from Díaz-González et al. (2023) at the resolution of the N_2H^+ data. We determine that in this V-shape the total $N(H_2)$ $\sim 1.03 \times 10^{26}$ cm^{-2}. Here, we derive a $M(H_2)$ map using Eq. 7:

$$M(H_2) = 2 \times N(H_2) \times {\rm area_{pixel}} \times {\rm m_{proton}}, \tag{7}$$

where from this $M(H_2)$ map we consider only the points that are part of the V-shape. To determine the mass associated to flowing motions we subtract the core masses (from Louvet et al. submitted) that are located inside this V-shape. Note here that this mass map is an upper limit given that we do not apply a background correction. We obtain a total of $M(H_2)$ ~ 54 $M_\odot$. Considering $t_{VG\ mean}$ used in Eq. 6, we derive the $\dot{M}_{\rm in}$ (H_2) as:

$$\dot{M}_{in}(H_2) = \frac{M(H_2)}{t_{VG\ mean}} = 8.32 \times 10^{-4}\ M_\odot\ {\rm yr}^{-1}. \tag{8}$$

We use the procedure described in this section to estimate the $\dot{M}_{\rm in}$ (H_2) of other eight V-shapes shown in Fig. D.2. We include these values in Table D.1. The average $\dot{M}_{\rm in}$ (H_2) of these V-shapes is $3.4 \times 10^{-4}\,M_\odot\,yr^{-1}$. We estimate the free-fall time of all 45 1.3 mm cores from Louvet et al. (submitted). These values present large scattering, ranging from (0.07 – 25) × $10^{-4}\,M_\odot\,yr^{-1}$, with 28 of these cores presenting $\dot{M}_{in}$ (H_2) < $10^{-4}\,M_\odot\,yr^{-1}$. For cores 2 & 3, the average $\dot{M}_{in}$ (H_2) is $15.5 \times 10^{-4}\,M_\odot\,yr^{-1}$, about twice the $\dot{M}_{in}$ (H_2) of the main blue V-shape, located between these two cores.

7.3. N_2H^+ relative abundance

For the main blue V-shape (Fig. D), we derive the N_2H^+ relative abundance $X(N_2H^+)$, using the N_2H^+ and H_2 column densities obtained above, as:

$$X(N_2H^+) = \frac{N(N_2H^+)}{N(H_2)} = 5.1 \times 10^{-10}. \quad (9)$$

The $X(N_2H^+)$ value obtained above is consistent, within the scatter, with other estimates in massive Galactic star formation regions in the ranges of (1.6 - 3.8) × 10^{-10} (Caselli et al. 2002a; Henshaw et al. 2014, Sandoval-Garrido et al. in prep.).

8. Discussion

The V-shaped velocity gradients described in this work have been detected across multiple Galactic star forming system. Stutz & Gould (2016) introduced the Slingshot mechanism in the Integral Shaped Filament (ISF) located in Orion A. They show undulations of the region in both position and velocity, suggesting that these features appear to be ejecting protostars (see their Fig. 2). Furthermore, Stutz (2018) characterize a standing wave in the neighborhood of the ISF, consistent with the Slingshot mechanism. It is possible that the undulations in the works above might result in the observed V-shaped structures seen in different studies (see below). González Lobos & Stutz (2019) identify six evenly spaced (every ∼ 0.44 pc) velocity peaks along the spine of the ISF in Orion A. They suggest that this periodicity is consistent with the wave-like perturbation in the gas caused by the Slingshot mechanism. In Álvarez-Gutiérrez et al. (2021) they analyze the L1482 filament located in the California Molecular Cloud. In all of the analyzed tracers there is a clear velocity peak in their north region (length ∼ 1.8 pc, mass ∼ $10^3\,M_\odot$). This subregion contains a higher gas density and higher number of YSOs compared to the more quiescent south part.

While the two regions described above are considered nearby (both at D ≲ 500 pc), more distant regions also present these velocity features which we list below. Zhou et al. (2022) study the velocity profiles along filaments from the ATOMS survey (Liu et al. 2020b). The median mass of their sources is ∼ $1.4 \times 10^3\,M_\odot$ with a median length of the filaments at ∼ 1.35 pc. By analyzing the $H^{13}CO^+$ (1−0) emission they find converging VGs along filaments (see their Figs. 6 & 10), which they also detected using simulations from Gómez & Vázquez-Semadeni (2014). These VGs at scales comparables to the V-shapes presented here are consistent with our VGs estimates (see their Fig. 7 & 8). In Zhou et al. (2023) they analyzed ^{13}CO (2−1) APEX/LAsMA data of the G333 complex. They identify multiple V-shaped VG (see their Fig. 7) which they describe as the PV projection of a funneling structure in PPV space (see their Fig. 9). The origin of this structure is due to material inflowing towards the central hub and also due to gravitational contraction of star-forming clouds or clumps.

Redaelli et al. (2022) use ALMA N_2H^+ (1−0) isolated component data of the high-mass (5200 $M_\odot$) clump AGAL014.492-00.139 identifying multiple coherent structures in PPV space (trees “B” and “G”; right panel of their Fig. 7 & 9). These are characterized by multiple undulations, and possible V-shaped VGs. For their “G” PV distribution, they suggest that one scenario is where the dense gas is flowing along the filament (of length ∼ 0.2 pc) from protostar “p3” towards the protostar “p2”. This motion has an $\dot{M}_{in}$ = $2.2 \times 10^{-4}\,M_\odot\,yr^{-1}$, being in the range of the $\dot{M}_{in}$ we derive for our VGs (see Table D.1).

In Rawat et al. (2024) they analyze ^{13}CO(1−0) ALMA data observing a V-shaped VG (see their Fig. 14) along the ridge of the G148.24+00.41 (G148) cloud. This V-shape peaks towards the dense clump at the center of this region, possibly indicating gas inflow along their filaments F2 and F6 towards the hub. Note that the length of the V-shape in G148 is ∼ 15 pc, while our most prominent V-shape (Fig. 10) span and lengths of their identified filaments are 1.3 to $6.9 \times 10^3\,M_\odot$ and 14 to 38 pc respectively, large compared to the total mass ($2.5 \times 10^3\,M_\odot$) and extent of G353 (∼ 1.2 pc). This different in probed length and masses might be reflected by their mean VG ∼ 0.05 km s^{-1} pc^{-1}, ∼ 2.5 orders of magnitude smaller than our VGs.

In Pan et al. (2024) using APEX $C^{18}O$ (2−1) data of the filamentary cloud G034.43+00.24 (G34) they identify converging VGs of lengths ∼ 1 pc towards the “middle ridge” see their Fig. 3, top panel). They interpret these VG as gas flowing from the filaments onto dense clumps, located at the center of G34. These VGs of their southern and northern filaments are in the range of ∼ 0.3−0.4 km s^{-1} pc^{-1}, and they estimate the total mass inflow rate towards the middle ridge as ∼ 5.5 × $10^{-4}\,M_\odot\,yr^{-1}$, similar to our $\dot{M}_{in}$ estimates.

Current work by Sandoval-Garrido et al. (in prep.) in G351.77 (intermediate protocluster, located at 2 kpc; Motte et al. 2022; Reyes-Reyes et al. 2024) use a similar analysis as we present in this work, where they identify multiple V-shaped velocity structures. In Salinas et al. (in prep) they analyze the kinematics of the evolved protocluster G012.80 (located at 2.4 kpc; Motte et al. 2022), where they implement similar techniques and find velocity signatures of filamentary rotation.

As presented here, V-shaped VGs appear to be a generic feature across a wide range of star forming environments, probing VGs with differences of up to ∼ 2 orders of magnitude in spatial scales ranging from 0.1 to ∼ 10 pc. Based on these works, the V-shaped VGs appear to be a generic feature in star forming regions. Despite being commonly detected in recent studies, it is still not clear how they are produced. Henshaw et al. (2014) highlights the degeneracy regarding the opposite interpretations of these V-shaped velocity structures. They suggest that these VGs can be a signature of gas flows along kinked filaments towards a core located at their convergence point. From our analysis regarding the most prominent V-shape (see § 5.3 & 6) we see that no core is located at its apex, although cores 2 & 3 are within ∼ 0.05 pc. Also the position difference between the center of the V-shape with the barycenter between these two cores is ∼ 600 AU. This is consistent with the idea of small-scale gravitational collapse within the protocluster, similar to clump decoupling from their parent molecular cloud (Peretto et al. 2023). Based on this, we conclude that cores may be located in the vicinity of the velocity apex, and not necessarily on top of it. These gas flows towards denser regions may result in the formation of high-mass cores in later stages during the evolution of the protocluster.

Regarding the kinked morphology of the regions hosting V-shapes, one scenario regarding magnetized shocks is presented in Inoue & Fukui (2013) and Inoue et al. (2018). They use magnetohydrodynamics simulations to characterize the interaction of molecular clouds and a magnetized shock produced by a cloud-

cloud collision. They find that the shock layer decelerates as it collides with denser regions. This deceleration reshapes the shock layer to be oblique, leading to the formation of kinked filaments and converging flows, which are oriented towards the apex of these filaments. They predict that magnetic fields present in the region should be perpendicular to these filaments and bend with the shock around the filament (Inoue et al. 2018, see their Fig. 3). In Bonne et al. (2020) and Bonne et al. (2023) they propose that this scenario takes place in the Musca and the DR21 filaments. In both of these regions they detect V-shaped VGs which they suggest are the result of cloud-cloud collisions bending the magnetic field (Bonne et al. 2020, see their Fig. 22 & 23). Further observations of magnetic field polarization in the POS, along with information along the line of sight is required to evaluate these models.

Another possibility is that these kinked structures could be caused by mechanisms such as the Slingshot. This mechanism proposes a standing wave, longitudinal gravitational instabilities, or large scale oscillations possibly caused by a possibly helical magnetic field morphology, causing ejections of protostars and protoclusters from their maternal filament (Stutz & Gould 2016; Stutz 2018; Stutz et al. 2018; Liu et al. 2019).

A different interpretation is that they are the product of outflowing material coming from a forming protostar interacting with the surrounding dense gas (see their Fig. 12). To shed light into this degeneracy in G353 we compare the N_2H^+ (dense gas tracer) radial velocities and SiO (shock/outflow tracer) as a proxy for energies. The velocity range ΔV covered by the N_2H^+ emission is ~ 8 km s^{-1}, while for SiO is ~ 80 km s^{-1}. Given the difference in probed velocities between SiO and N_2H^+ (see § 5.3) and the analysis presented in § 6 we suggest that the V-shapes in G353 are a signature of infall.

As presented in this section, the V-shaped VGs appear to be common in recent studies of protoclusters. The multiple VGs that conform the V-shapes present in G353 have values of $\sim$ 8 to $\sim$ 31 km s^{-1} pc^{-1}, with timescales ranging from $\sim$ 35 to 173 kyr, and $\dot{M}_{\rm in}$ values $(\sim 0.4 - 9) \times 10^{-4}\,M_\odot\,{\rm yr}^{-1}$. These values are similar to VGs in other regions with comparable sizes and masses. In G353 it is likely that these VGs are the result of dense gas moving through filaments, possibly increasing the density of the central regions, shaping the overall velocity field at large and small scales, and leading to a further increase of the core population and star formation activity.

One important aspect of the V-shapes that is still not well understood is the timescale associated of the VGs ($t_{VG} = {\rm VG}^{-1}$). It is not clear if nor how these timescales determine core formation lifetimes or impact the star formation environment in general. In our sample of V-shapes the timescales are in tens of kyrs with the average value of $\sim$ 67 kyr, $\sim$ 2 times the cores t_{ff}, while the t_{ff} of the whole protocluster is $\sim$ 0.21 Myr. In Rawat et al. (2024) they estimate the longitudinal collapse timescales for their filaments, being in the range of 5 – 15 Myr. Using their derived VGs we estimate their associated timescales to be between $\sim$ 16 and $\sim$ 50 Myr, $\sim$ 1 – 2 orders of magnitude larger than our small scale V-shapes timescales. We suggest that the VG timescales might serve as an upper limit for filamentary collapse timescales. In Zhou et al. (2022) they determine gas accretion times as a function of the lengths of their filaments, assuming that the VGs produced by gas inflow (see their Fig. 11). At filament lengths comparable to our V-shapes ($\sim$ 0.1 pc) their gas accretion timescales are on the order of our estimates (see Table D.1).

It is also interesting to consider the mass accretion rates measured here compared to the available protocluster mass reservoir to explore implications for the duration of the gas dominated phase. The total mass accretion rate of our V-shaped structures is $\dot{M}_{\rm in,\,Tot} = 3 \times 10^{-3}\,M_\odot\,{\rm yr}^{-1}$ (see Table D.1). Considering the total mass ($M_{\rm Tot}$) of G353 as a mass reservoir, we estimate the time needed fully consume the gas (t_{cons}). Here we assume that $\dot{M}_{\rm in,\,Tot}$ is representative of flows feeding gas onto cores. We estimate $t_{cons} = M_{\rm Tot}/\dot{M}_{\rm in,\,Tot}$, where the total mass of the region is 2500 $M_\odot$ (Motte et al. 2022). We obtain a $t_{cons} = 0.8$ Myr, of similar magnitude but about four times larger than the t_{ff} of the protocluster. Considering that our estimate of $\dot{M}_{\rm in,\,Tot}$ is certainly a lower limit (see discussion above), the actual value value of t_{cons} is likely to be shorter, so closer to the free-fall time estimate. Given that the protocluster does not appear to be in a state of free-fall (see § 6) but instead undergoing comparatively slow gravitational contraction, the similarity in these relatively crude estimates seems remarkable. While we do not yet have an explanation for why this relatively good match in timescales, it would seem to indicate that protocluster evolution may be a self-regulating process. Larger samples and similar analysis will test this hypothesis.

Moreover, the approximate concordance of t_{cons} and t_{ff} may indicate that the "phase transition" of protocluster gas mass being converted into stellar mass could contribute a relevant "negative pressure" counteracting effects of e.g. feedback over the lifetime of the protocluster.

9. Summary & conclusions

We characterize the complex dense gas kinematics of G353 using ALMA-IMF LP observations. The data used in this paper mainly consist of the fully combined N_2H^+ data cube, but we also include 1.3 mm continuum cores and DCN cores velocity catalogues, SiO 12 m observation, and a $N(H_2)$ 1.3 mm continuum derived map. We summarize our main results below.

1. With our N_2H^+ isolated component modeling, we find that most of the 1.3 mm cores are located in regions with 2 to 3 velocity components. This indicates kinematic complexity down to ~4 kau scales.
2. We increase the number of cores with a $V_{\rm LSR}$ estimate in this region by further examining the DCN emission and comparing it with the N_2H^+ data extracted towards the core positions. We find that 11 cores, which were previously undetected in the in the DCN background-subtracted fitting from Cunningham et al. (2023), are identified with our method. With this approach we increase our core velocities sample from 15 to 26, accounting for $\sim$ 58% of the total 45 1.3 mm continuum cores. These are presented in Table C.1.
3. We show that the traditional PV diagram highlights large, protocluster scale kinematics. In contrast, the intensity-weighted PV diagram allows us access to the small, core scale dynamics (see Figs. 8 and 9).
4. From the PV diagrams, we see the DCN core velocities are in agreement with the N_2H^+ velocity distribution (within a few DCN channel widths). This suggests coupling between the cores and the dense gas in which they formed.
5. In the intensity-weighted PVs we see clear V-shaped velocity structures, composed by two linear velocity gradients (VGs) converging into a common point. These VGs are present across all N_2H^+ velocity components. Some of them are near the location of cores in both position and velocity (see § 5.2)
6. We successfully characterize nine V-shaped VGs well detected in our N_2H^+ data (see Fig. D.2).

7. V-shape "C" (see Fig. 10, 11, and 12) is the most prominent across our sample. It is centered between cores 2 and 3, two of the most massive cores in this region.
8. We estimate the barycenter of cores 2 & 3, presenting an offset relative to the center of the V-shape of $\sim 0.3''(\sim 600\,\mathrm{au})$ well below the beam size of our N_2H^+ data.
9. For V-shape "B" we find that core "7", with a mass of $6\,M_\odot$, is located within a ~beam size from its apex.
10. We suggest that the dense gas is flowing along the filament, producing the V-shaped structure towards the derived barycenter.
11. We characterize the VGs composing our sample of V-shapes by applying linear fits to these distributions. We estimate timescales associated to the VGs as $t_{VG} = \mathrm{VG}^{-1}$. These timescales are between ~35 to ~170 kyr, with an average of ~67 kyr. These values are short compared to the t_{ff} of the protocluster (~ 0.21 Myr), and ~ 2 times larger that the cores average t_{ff} (~ 32 kyr).
12. We suggest that at small scales the N_2H^+ V-shaped structures indicate gas motions along filaments, towards denser regions.
13. Using an H_2 mass map and the V-shapes mean timescales, we derive H_2 mass accretion rates of $(0.35\,\mathrm{to}\,8.77) \times 10^{-4}\ M_\odot\ \mathrm{yr}^{-1}$, consistent with previous studies on regions that present gas flows along filaments towards denser object or regions, such as protostars and clumps.
14. In SiO, the PV structure covers a velocity range (ΔV) of $\sim$ 80 km s^{-1}, while for N_2H^+ ΔV is $\sim$ 8 km s^{-1}. This difference suggests that N_2H^+ is tracing infall, a less energetic processes compared to SiO, a shock and outflow tracer.
15. We model a gravitationally collapsing sphere. The derived radial velocities are consistent with the large scale morphology of the traditional PV diagram. This agreement suggests that at large scales the G353 protocluster is undergoing gravitational contraction.

Overall, it is imperative to replicate the kinematic analysis presented in this work in the remaining ALMA-IMF fields and other Galactic star forming regions. By increasing the sample of analyzed fields we might find correlations between evolutionary state (young, intermediate, or evolved; see Motte et al. 2022), star formation activity, cores and outflow population properties, and their velocity field. This approach will allow us to better describe the kinematic processes taking place in this early stage of star formation.

Acknowledgements. This paper makes use of the following ALMA data: ADS/JAO.ALMA#2017.1.01355.L. ALMA is a partnership of ESO (representing its member states), NSF (USA) and NINS (Japan), together with NRC (Canada), MOST and ASIAA (Taiwan), and KASI (Republic of Korea), in cooperation with the Republic of Chile. The Joint ALMA Observatory is operated by ESO, AUI/NRAO and NAOJ. We thank Elena Redaelli and Diego R. Matus Carrillo for very helpful discussions. R.A. gratefully acknowledges support from ANID Beca Doctorado Nacional 21200897. A.S. gratefully acknowledges support by the Fondecyt Regular (project code 1220610) and ANID BASAL project FB210003. F.L. acknowledges the support of the Marie Curie Action of the European Union (project *MagiKStar*, Grant agreement number 841276) F.M. acknowledges support from the French Agence Nationale de la Recherche (ANR) under reference ANR-20-CE31-009, of the Programme National de Physique Stellaire and Physique et Chimie du Milieu Interstellaire (PNPS and PCMI) of CNRS/INSU (with INC/INP/IN2P3). R.G.M. and D.D.G. acknowledge support from UNAM-PAPIIT project IN108822 and from CONACyT Ciencia de Frontera project ID 86372. F.M., F.L., and N.C. acknowledge support from the European Research Council (ERC) via the ERC Synergy Grant ECOGAL (grant 855130). N.C. acknowledges funding from the ERC under the European Union's Horizon 2020 research. P.S. was partially supported by a Grant-in-Aid for Scientific Research (KAKENHI Number JP22H01271 and JP23H01221) of JSPS. M.B. is a postdoctoral fellow in the University of Virginia's VICO collaboration and is funded by grants from the NASA Astrophysics Theory Program (grant number 80NSSC18K0558) and the NSF Astronomy & Astrophysics program (grant number 2206516). T.Cs. has received financial support from the French State in the framework of the IdEx Université de Bordeaux Investments for the future Program. S.D.R. acknowledges the funding and support of ANID-Subdirección de Capital Humano Magíster/Nacional/2021-22211000. T.B. acknowledges the support from S. N. Bose National Centre for Basic Sciences under the Department of Science and Technology, Govt. of India. G.B. acknowledges financial support from the grants PID2020-117710GB-I00 and CEX2019-000918 funded by MCIN/AEI/10.13039/501100011033. A.K. and L.B. gratefully acknowledge support from ANID BASAL project FB210003. F.O. acknowledge the support of the Ministry of Science and Technology of Taiwan, projects No. 109-2112-M-007-008-, 110-2112-M-007-023-, and 110-2112-M-007-034-.

References

Álvarez-Gutiérrez, R. H., Stutz, A. M., Law, C. Y., et al. 2021, ApJ, 908, 86
André, P., Men'shchikov, A., Bontemps, S., et al. 2010, A&A, 518, L102
Anglada, G., Rodriguez, L. F., Canto, J., Estalella, R., & Lopez, R. 1987, A&A, 186, 280
Armante, M., Gusdorf, A., Louvet, F., et al. 2024, arXiv e-prints, arXiv:2401.09203
Bastian, N., Covey, K. R., & Meyer, M. R. 2010, ARA&A, 48, 339
Bergin, E. A., Alves, J., Huard, T., & Lada, C. J. 2002, ApJ, 570, L101
Bonfand, M., Csengeri, T., Bontemps, S., et al. 2024, arXiv e-prints, arXiv:2402.15023
Bonne, L., Bontemps, S., Schneider, N., et al. 2020, A&A, 644, A27
Bonne, L., Bontemps, S., Schneider, N., et al. 2023, ApJ, 951, 39
Busquet, G., Zhang, Q., Palau, A., et al. 2013, ApJ, 764, L26
Caselli, P., Benson, P. J., Myers, P. C., & Tafalla, M. 2002a, ApJ, 572, 238
Caselli, P., Myers, P. C., & Thaddeus, P. 1995, ApJ, 455, L77
Caselli, P., Walmsley, C. M., Zucconi, A., et al. 2002b, ApJ, 565, 344
Cazzoli, G., Corbelli, G., Degli Esposti, C., & Favero, P. 1985, Chemical Physics Letters, 118, 164
Chen, H.-R. V., Zhang, Q., Wright, M. C. H., et al. 2019, ApJ, 875, 24
Csengeri, T., Bontemps, S., Schneider, N., Motte, F., & Dib, S. 2011, A&A, 527, A135
Csengeri, T., Bontemps, S., Wyrowski, F., et al. 2017, A&A, 601, A60
Cunningham, N., Ginsburg, A., Galván-Madrid, R., et al. 2023, A&A, 678, A194
Cunningham, N., Lumsden, S. L., Cyganowski, C. J., Maud, L. T., & Purcell, C. 2016, MNRAS, 458, 1742
Díaz-González, D. J., Galván-Madrid, R., Ginsburg, A., et al. 2023, ApJS, 269, 55
Fernández-López, M., Arce, H. G., Looney, L., et al. 2014, ApJ, 790, L19
Ginsburg, A. & Mirocha, J. 2011, PySpecKit: Python Spectroscopic Toolkit, Ver. 0.1.23, Astrophysics Source Code Library
Ginsburg, A., Sokolov, V., de Val-Borro, M., et al. 2022, AJ, 163, 291
Gómez, G. C. & Vázquez-Semadeni, E. 2014, ApJ, 791, 124
González Lobos, V. & Stutz, A. M. 2019, MNRAS, 489, 4771
Hacar, A., Tafalla, M., Forbrich, J., et al. 2018, A&A, 610, A77
Henshaw, J. D., Caselli, P., Fontani, F., Jiménez-Serra, I., & Tan, J. C. 2014, MNRAS, 440, 2860
Henshaw, J. D., Ginsburg, A., Haworth, T. J., et al. 2019, MNRAS, 485, 2457
Inoue, T. & Fukui, Y. 2013, ApJ, 774, L31
Inoue, T., Hennebelle, P., Fukui, Y., et al. 2018, PASJ, 70, S53
Koch, E. W. & Rosolowsky, E. W. 2015, MNRAS, 452, 3435
Kuznetsova, A., Hartmann, L., & Ballesteros-Paredes, J. 2015, ApJ, 815, 27
Kuznetsova, A., Hartmann, L., & Ballesteros-Paredes, J. 2018, MNRAS, 473, 2372
Lee, C. W., Myers, P. C., & Tafalla, M. 1999, ApJ, 526, 788
Lee, C. W., Myers, P. C., & Tafalla, M. 2001, ApJS, 136, 703
Lippok, N., Launhardt, R., Semenov, D., et al. 2013, A&A, 560, A41
Liu, H. B., Galván-Madrid, R., Jiménez-Serra, I., et al. 2015, ApJ, 804, 37
Liu, H.-L., Stutz, A., & Yuan, J.-H. 2019, MNRAS, 487, 1259
Liu, T., Evans, N. J., Kim, K.-T., et al. 2020a, MNRAS, 496, 2790
Liu, T., Evans, N. J., Kim, K.-T., et al. 2020b, MNRAS, 496, 2790
Mardones, D., Myers, P. C., Tafalla, M., et al. 1997, ApJ, 489, 719
Minh, Y. C., Liu, H. B., Galvań-Madrid, R., et al. 2018, ApJ, 864, 102
Motte, F., Bontemps, S., Csengeri, T., et al. 2022, A&A, 662, A8
Motte, F., Bontemps, S., & Louvet, F. 2018, ARA&A, 56, 41
Nony, T., Galván-Madrid, R., Motte, F., et al. 2023, A&A, 674, A75
Offner, S. S. R., Clark, P. C., Hennebelle, P., et al. 2014, in Protostars and Planets VI, ed. H. Beuther, R. S. Klessen, C. P. Dullemond, & T. Henning, 53–75
Olguin, F. A., Sanhueza, P., Chen, H.-R. V., et al. 2023, ApJ, 959, L31
Pan, S., Liu, H.-L., & Qin, S.-L. 2024, ApJ, 960, 76
Peretto, N., Rigby, A. J., Louvet, F., et al. 2023, MNRAS, 525, 2935
Pouteau, Y., Motte, F., Nony, T., et al. 2022, arXiv e-prints, arXiv:2212.09307
Rawat, V., Samal, M. R., Walker, D. L., et al. 2024, MNRAS[`arXiv:2401.03202`]
Redaelli, E., Bovino, S., Sanhueza, P., et al. 2022, ApJ, 936, 169

Reyes-Reyes, S. D., Stutz, A. M., Megeath, S. T., et al. 2024, MNRAS[`arXiv:2403.02456`]
Sanhueza, P., Contreras, Y., Wu, B., et al. 2019, ApJ, 886, 102
Sanhueza, P., Girart, J. M., Padovani, M., et al. 2021, ApJ, 915, L10
Schuller, F., Menten, K. M., Contreras, Y., et al. 2009, A&A, 504, 415
Smith, R. J., Shetty, R., Stutz, A. M., & Klessen, R. S. 2012, ApJ, 750, 64
Storm, S., Mundy, L. G., Fernández-López, M., et al. 2014, ApJ, 794, 165
Stutz, A. M. 2018, MNRAS, 473, 4890
Stutz, A. M., Gonzalez-Lobos, V. I., & Gould, A. 2018, arXiv e-prints, arXiv:1807.11496
Stutz, A. M. & Gould, A. 2016, A&A, 590, A2
Stutz, A. M. & Kainulainen, J. 2015, A&A, 577, L6
Tafalla, M., Myers, P. C., Caselli, P., & Walmsley, C. M. 2004, A&A, 416, 191
Tobin, J. J., Hartmann, L., Bergin, E., et al. 2012, ApJ, 748, 16
Towner, A. P. M., Ginsburg, A., Dell'Ova, P., et al. 2024, ApJ, 960, 48
Ungerechts, H., Bergin, E. A., Goldsmith, P. F., et al. 1997, ApJ, 482, 245
Wienen, M., Wyrowski, F., Menten, K. M., et al. 2015, A&A, 579, A91
Zhou, J.-W., Liu, T., Evans, N. J., et al. 2022, MNRAS, 514, 6038
Zhou, J. W., Wyrowski, F., Neupane, S., et al. 2023, A&A, 676, A69

---

[1] Departamento de Astronomía, Universidad de Concepción, Casilla 160-C, Concepción, Chile e-mail: `rodralvarezz@gmail.com`
[2] Univ. Grenoble Alpes, CNRS, IPAG, 38000 Grenoble, France
[3] Instituto de Radioastronomía y Astrofísica, Universidad Nacional Autónoma de México, Morelia, Michoacán 58089, México
[4] SKA ObservatoryJodrell Bank, Lower Withington, Macclesfield, SK11 9FT, United Kingdom
[5] National Astronomical Observatory of Japan, 2-21-1 Osawa, Mitaka, Tokyo 181-8588, Japan
[6] Astronomical Science Program, The Graduate University for Advanced Studies, SOKENDAI, 2-21-1 Osawa, Mitaka, Tokyo 181-8588, Japan
[7] Departments of Astronomy, University of Virginia, Charlottesville, VA 22904, USA
[8] Laboratoire d'astrophysique de Bordeaux, Univ. Bordeaux, CNRS, B18N, allée Geoffroy Saint-Hilaire, F-33615 Pessac, France
[9] Laboratoire de Physique de l'École Normale Supérieure, ENS, Université PSL, CNRS, Sorbonne Université, Université Paris Cité, F-75005, Paris, France
[10] Observatoire de Paris, PSL University, Sorbonne Université, LERMA, 75014, Paris, France
[11] Max Planck Institute for Astronomy, Königstuhl 17, 69117 Heidelberg, Germany
[12] S. N. Bose National Centre for Basic Sciences, Sector-III, Salt Lake, Kolkata 700106, India
[13] Astronomy Department, Universidad de Chile, Camino El Observatorio 1515, Las Condes, Santiago, Chile
[14] Departament de Física Quàntica i Astrofísica (FQA), Universitat de Barcelona (UB), Martí i Franquès 1, 08028 Barcelona, Catalonia, Spain
[15] Institut de Ciències del Cosmos (ICCUB), Universitat de Barcelona, Martí i Franquès, 1, 08028, Barcelona, Catalonia, Spain
[16] Institut d'Estudis Espacials de Catalunya (IEEC), Gran Capità, 2-4, 08034 Barcelona, Catalonia, Spain
[17] Instituto Argentino de Radioastronomía (CCT-La Plata, CONICET; CICPBA), C.C. No. 5, 1894, Villa Elisa, Buenos Aires, Argentina
[18] Joint Alma Observatory (JAO), Alonso de Córdova 3107, Vitacura, Santiago, Chile
[19] School of Physics and Astronomy, Yunnan University, Kunming, 650091, People's Republic of China
[20] Institute of Astronomy and Department of Physics, National Tsing Hua University, Hsinchu 30013, Taiwan
[21] Max-Planck-Institut für Radioastronomie, Auf dem Hügel 69, 53121 Bonn, Germany

Appendix A: Filamentary identification with FilFinder

Here we describe the procedure to identify the main filamentary structures presented in § 3 using `FilFinder` (Koch & Rosolowsky 2015).

For this approach we use the moment 0 map of the extracted N_2H^+ isolated components that present a SNR ≥ 5. To estimate the moment 0 map we used the `moment` task from the `SpectralCube` Python package, within the velocity range of -31.5 km s^{-1} to 0 km s^{-1}. As part of the pre-processing of the moment 0 map before the filamentary detection, we decrease the contrast in the image by using the `preprocess_image` task and its argument `flatten_percent` set to 90. Now, in order to indicate to `FilFinder` the area we to identify filaments use the subtask `create_mask` with the following parameters: `glob_thresh: 4.5 K km s`$^{-1}$, `size_thresh: 0.25 pc`^{2}, `smooth_size: 0.12 pc`, `border_masking: False`, `fill_hole_size: 0.013 pc`^{2}. The resulting mask is presented in Fig. A.1 with a white contour.

Then, we obtain the skeletons of the mask by using `medskel`. The derived structures are presented with red and black lines in Fig. A.1. Given we are only interested in the large scale filaments, we use `analyze_skeletons` in order to "prune" the small scale structures. For this pruning we use `branch_thresh: 0.3 pc`, `prune_criteria: 'length'`, `max_prune_iter: 0`. This approach results in removing the small filaments (red lines in Fig. A.1) from the original skeleton and to obtain the main filamentary structure in G353 (black lines in Fig. A.1).

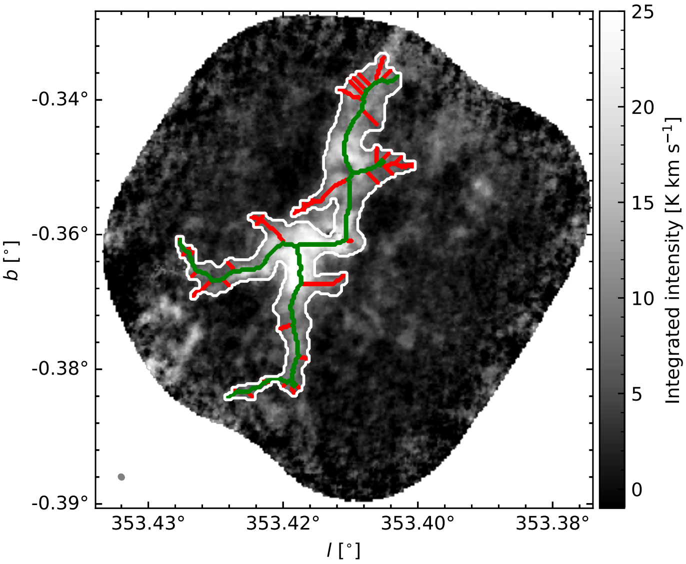

Fig. A.1: `FilFinder` filamentary identification. The background indicates the moment 0 map of the extracted N_2H^+ isolated components. The white contour shows the area where `FilFinder` identifies multiple filamentary structures (red and green lines). We remove the small scale structures (in red) by "pruning" the skeleton structure from `medskel`, obtaining the main filaments of G353. We represent these filaments with green lines.

Appendix B: Examples of the isolated components fitting

In § 3 we decomposed the multiple isolated component emission using `PySpecKit`. In Fig. B.1 we present the results of the Gaussian fitting for the high SNR spectra shown in Fig. 3 (panels c, d, and e).

Appendix C: DCN & N_2H^+ derived core velocity

In Table C.1 we provide the 1.3 mm core velocities obtained from DCN & N_2H^+ data (see § 4.1), complementing the published DCN core velocities catalogue from Cunningham et al. (2023).

Appendix D: V-shaped structures

In § 5.3 we characterized the most prominent V-shaped structure we detect in Fig. 9. We repeat this process for other eight different V-shaped structures, including the linear fits to the velocity gradients. In Fig. D.1 we indicate their location in PV space with arrows and present individual close-up for each V-shape in Fig. D.2. In Table D.1 we list their VGs, timescales, H_2 masses, and mass accretion rates.

Here we list a few clarifications due to projection effects seen in these V-shaped structures:

- In position-position space, only V-shape "B" presents a core within a ~beam size from its apex.
- For V-shape "A", the 1.3 mm core with DCN single velocity component, located at the apex of this V-shape, is not spatially related to it.
- In V-shapes "G" and "H" we see the same 1.3 mm cores with N_2H^+ velocities. These V-shapes are not the same distribution. They are overlapped in PV space and spatially separated by $\sim 10''$.
- We improve the clarity of V-shape "B" by rotating the data in PP space by 80° counter-clockwise. We apply this process for V-shapes "E", "G", and "H" with an angle of 33° clockwise.
- V-shapes G and H overlap in PV space but these are structures spatially separated.

Appendix E: SiO Intensity-weighted position-velocity diagram

To create the SiO intensity-weighted PV diagram, first, we remove most of the noisy spectra by considering data with SNR $\geq$ 2.5. Then, we estimate the integrated intensity and velocity centroid at each pixel. We find improvements in our cleaning by using only spectra with integrated intensity $\geq$ 4 K km s^{-1}. Using the coordinate, integrated-intensity, and velocity centroid of each spectrum, we create the SiO intensity-weighted PV diagrams we show in E.1.

Appendix F: G353 power law density profile

Here we provide the derivation of the density profile used for the gravitationally collapsing sphere. We assume a power law density profile defined as:

$$\rho(r) \quad = \quad \rho_0 \left(\frac{r}{\mathrm{pc}}\right)^{-\gamma}, \qquad \text{(F.1)}$$

where $\gamma = 5.65$ provides a good fit to the edges of the PV distribution seen in Fig. 8.

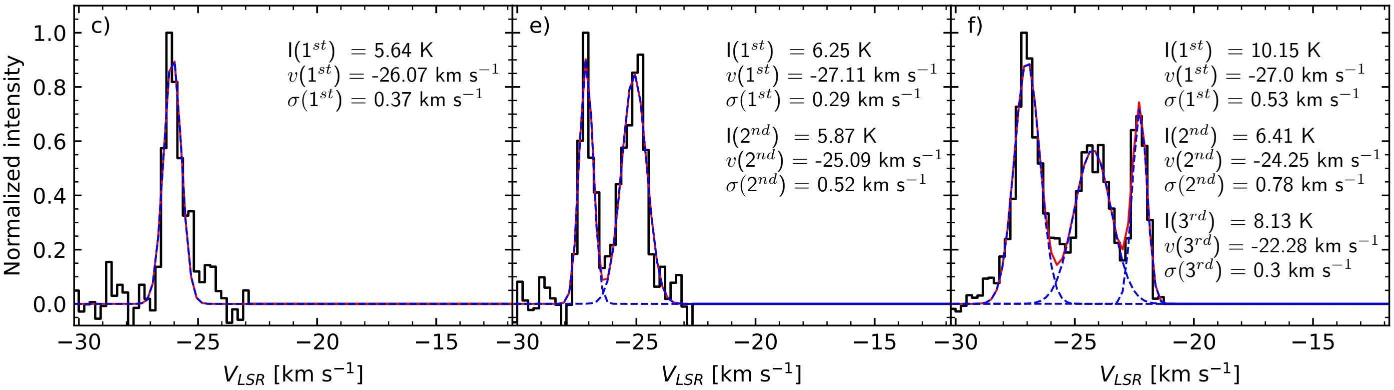

Fig. B.1: Gaussian velocity fits of the extracted N_2H^+ isolated components. In black we show the high SNR isolated components from panels c), e), and f) in Fig. 3. The individual Gaussian components and the obtained model are represented with dashed blue and solid red lines respectively. On the right side of each panel we indicate the peak intensity (I), the velocity centroid (v), and velocity dispersion (σ) of each Gaussian component. The notations 1^{st}, 2^{nd}, and 3^{rd} indicate the Gaussian velocity components from left to right.

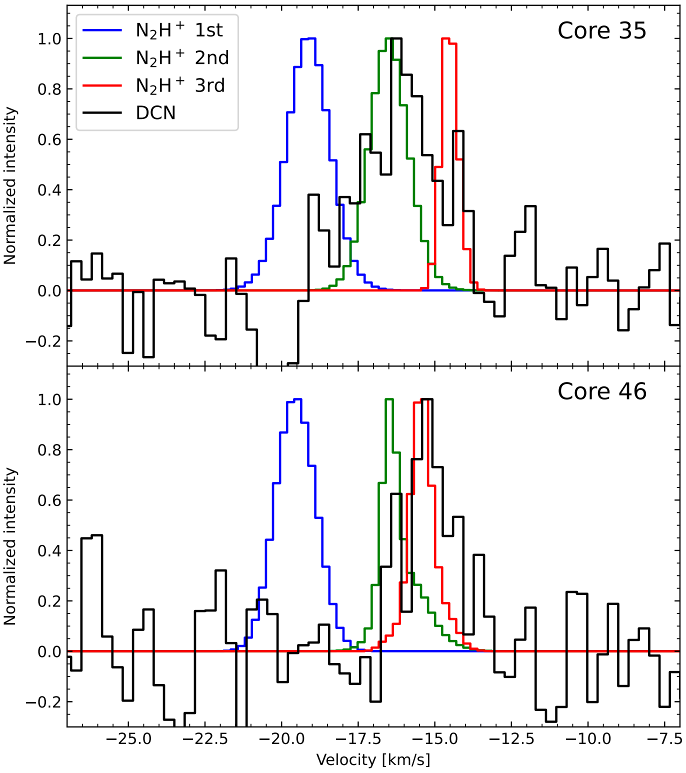

Fig. C.1: DCN and N_2H^+ normalized mean spectra of cores 35 (top) and 46 (bottom). We show the multiple N_2H^+ isolated velocity components with blue, red, and green colors. We present the DCN emission in black. We see a match between the DCN emission and one of the N_2H^+ velocity components. We determine the N_2H^+ velocity for 11 cores with no DCN velocity fits. These are listed in Table C.1.

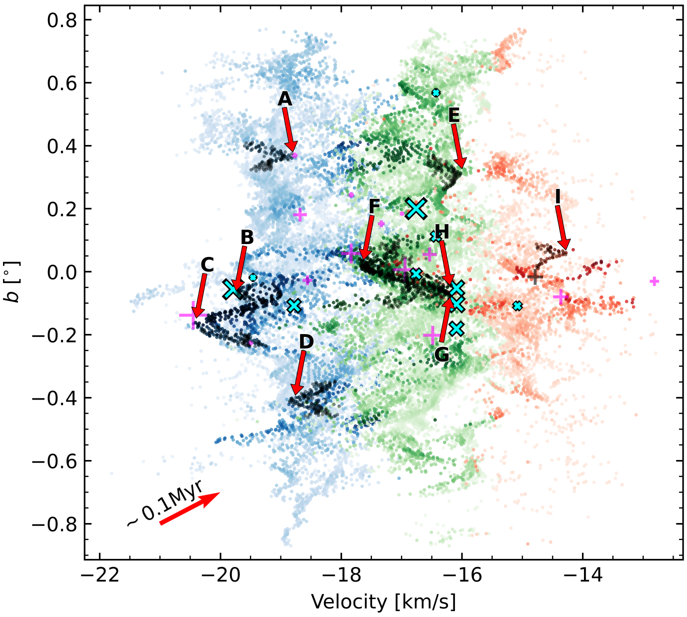

Fig. D.1: V-shapes location in PV space. In the background we show the Intensity-weighted position-velocity diagram from Fig. 9. We highlight the V-shapes listed in Table D.1 with black points and indicate them with red arrows and their ID. The DCN core velocities and the N_2H^+ velocity distributions follow the same definitions from the top right panel in Fig. D.1. V-shapes G and H overlap in PV space but these structures are spatially separated.

To determine the value of ρ_0, we integrate this expression in a sphere (Eq. F.2), with $r_{min} < r < 0.5$ pc. Based of different testings we set the total mass of the sphere to 150 $M_\odot$. We define $r_{min} \sim 0.007$ pc which corresponds to the pixel size of the N_2H^+ data at a distance of 2 kpc.

$$M_{enc}(r = 0.5\text{ pc}) = 4\pi\rho_0 \int_{r_{min}}^{0.5\text{ pc}} \left(\frac{r}{\text{pc}}\right)^{-\gamma} r^2 dr \tag{F.2}$$

$$= 4\pi\rho_0 \frac{r^{3-\gamma}}{3-\gamma}\Bigg|_{r\,=\,r_{min}}^{r\,=\,0.5\text{ pc}} \text{pc}^{\gamma} \tag{F.3}$$

$$= \frac{4\pi\rho_0}{3-\gamma}\left(0.5^{3-\gamma} - {r_{min}}^{3-\gamma}\right) \text{pc}^{\gamma}, \tag{F.4}$$

Table C.1: 1.3 mm core catalogue of DCN & N_2H^+ velocities

Core Number	RA [°]	DEC [°]	F_A [″]	F_B [″]	PA [°]	Mass [$M_\odot$]	V_{LSR} [km s^{-1}]	Type
2	262.6165032	-34.6955865	1.98	1.59	64.00	20.7	−20.45±0.065	DCN, Single
3	262.6184156	-34.6965240	2.59	1.79	146.00	9.4	−16.48±0.040	DCN, Single
4	262.6103159	-34.6932659	1.56	1.46	104.00	5.2	−16.53±0.155	DCN, Single
5	262.6101515	-34.6960014	2.03	1.75	79.00	16.0	−16.94±0.087	DCN, Single
6	262.6049155	-34.6934384	1.60	1.48	129.00	4.9	−18.68±0.126	DCN, Single
7	262.6137738	-34.6947298	1.63	1.27	80.99	6.0	−19.79	DCN & N_2H^+
8	262.6039531	-34.6936374	2.26	1.56	97.32	6.6	–	–
9	262.6192359	-34.6903650	2.69	1.96	62.96	3.7	−16.09	DCN & N_2H^+
11	262.6243189	-34.6880780	2.12	1.95	172.70	2.8	−16.09	DCN & N_2H^+
12	262.6072148	-34.6969795	2.98	2.02	86.00	10.3	−17.83±0.019	DCN, Single
13	262.6078228	-34.6996836	1.91	1.48	153.90	2.7	–	–
14	262.6147937	-34.6946762	2.00	1.58	124.00	6.2	−14.36±0.090	DCN, Single
15	262.6107433	-34.6964412	1.96	1.59	93.00	6.6	−14.78±0.087	DCN, Complex
16	262.6215941	-34.6989408	2.68	2.49	19.37	1.5	–	–
17	262.5954514	-34.6916168	1.57	1.42	87.50	0.9	–	–
18	262.5927434	-34.7052494	1.97	1.56	89.26	0.8	–	–
19	262.6064012	-34.7019756	1.55	1.20	57.74	0.5	–	–
20	262.6111096	-34.6932787	1.67	1.63	178.00	1.3	–	–
21	262.6131910	-34.6939495	2.10	1.48	108.00	2.4	−18.56±0.063	DCN, Single
22	262.6118441	-34.6946150	1.89	1.59	96.65	1.7	−16.76	DCN & N_2H^+
23	262.6028175	-34.6925438	1.84	1.31	112.70	0.8	–	–
24	262.6198349	-34.6960383	1.88	1.72	76.00	0.8	−19.50±0.089	DCN, Single
25	262.6155222	-34.6952591	1.87	1.20	137.30	2.5	−18.78	DCN & N_2H^+
26	262.6143434	-34.6917027	1.49	1.24	137.30	0.8	–	–
27	262.6000802	-34.6910324	3.39	2.51	48.16	1.8	–	–
28	262.6253977	-34.6999713	2.56	1.87	39.31	0.8	–	–
29	262.6133074	-34.6919187	1.67	1.26	76.67	0.7	–	–
30	262.6114686	-34.6962602	1.52	1.41	30.00	2.3	−12.81±0.074	DCN, Single
31	262.6096651	-34.6925680	1.72	1.34	119.10	0.7	–	–
32	262.6094126	-34.6910985	2.44	2.02	59.22	2.0	–	–
33	262.6287106	-34.6862068	2.32	2.00	16.64	1.7	–	–
34	262.5982914	-34.6919006	1.81	1.36	139.00	0.8	−18.77±0.080	DCN, Single
35	262.6142011	-34.6940134	2.31	1.81	111.00	3.4	−16.09	DCN & N_2H^+
36	262.6202758	-34.7001995	2.19	1.88	141.00	0.8	–	–
37	262.6010398	-34.6950114	1.74	1.33	75.00	0.8	−17.83±0.053	DCN, Single
38	262.5971034	-34.6920396	2.01	1.61	104.80	0.7	–	–
39	262.6054437	-34.6963773	2.05	1.88	158.50	1.4	−16.43	DCN & N_2H^+
40	262.5917454	-34.6897316	1.85	1.50	92.93	0.6	–	–
41	262.6095777	-34.6983259	2.23	1.83	72.51	1.3	–	–
42	262.5975992	-34.6876666	1.51	1.22	24.46	0.3	–	–
43	262.6035166	-34.6966807	2.48	1.78	95.00	1.2	−17.33±0.062	DCN, Single
44	262.6030115	-34.6956424	1.76	1.55	96.00	0.5	−16.99±0.091	DCN, Single
45	262.6143008	-34.6909376	3.40	2.75	94.93	2.6	–	–
46	262.6187648	-34.6912377	3.10	2.15	40.67	0.9	−15.08	DCN & N_2H^+
47	262.6178453	-34.6919943	3.09	2.48	45.43	1.6	–	–

Notes. Velocities of the 1.3 mm continuum derived cores. The column "Type" indicates if the core velocity is determined by a single or complex DCN spectra (Cunningham et al. 2023), or using both DCN & N_2H^+ data (this work). For completeness we include the properties of the 1.3 mm cores with no velocity determinations. These cores present a "–" in the last two columns.

where $M_{enc}(r = 0.5\,\mathrm{pc}) = 150\ \mathrm{M}_\odot$, $r_{min} = 7 \times 10^{-3}$ pc, and $\gamma = 5.65$, from Eq. F.4, we obtain:

$$\rightarrow \rho_0 = 6.1 \times 10^{-5} \frac{\mathrm{M}_\odot}{\mathrm{pc}^3}. \qquad \text{(F.5)}$$

Table D.1: Characterized V-shaped structures

V-shape ID	l [°]	b [°]	$M(H_2)$ [M$_\odot$]	Upper / lower VG [km s^{-1} pc^{-1}]	Mean VG [km s^{-1} pc^{-1}]	Upper / lower t_{VG} [kyr]	$t_{VG\ mean}$ [kyr]	$\dot{M}_{\rm in}(H_2)$ [10^{-4} M$_\odot$ yr^{-1}]
A	353.3981	-0.3506	7.50	20.85 / 17.04	18.95	46.89 / 57.39	52.14	1.43
B	353.4127	-0.3632	13.42	25.34 / 17.22	21.28	38.59 / 56.77	47.68	2.81
C	353.4135	-0.3657	53.74	17.69 / 13.26	15.48	55.28 / 73.75	64.52	8.32
D	353.4133	-0.3727	7.77	12.85 / 21.22	17.15	76.07 / 46.07	61.07	1.27
E	353.4096	-0.3521	6.16	12.47 / 3.63	8.05	78.38 / 269.57	173.98	0.35
F	353.4128	-0.3604	27.36	15.75 / 15.61	15.68	62.09 / 62.64	62.37	4.38
G	353.4110	-0.3630	3.32	22.59 / 24.46	23.53	43.29 / 39.97	41.63	0.79
H	353.4140	-0.3627	30.95	21.28 / 39.68	30.48	45.94 / 24.64	35.29	8.77
I	353.4091	-0.3595	15.94	22.34 / 11.22	16.78	43.77 / 87.17	65.47	2.43

Notes. Properties of the nine, well characterized, V-shaped structures identified in our N_2H^+ data. The coordinates indicate the position of the velocity apex of each V-shape. V-shape "C" represents the structure analyzed in § 5.3. We show the PV distribution of these structures in Fig. D.2.

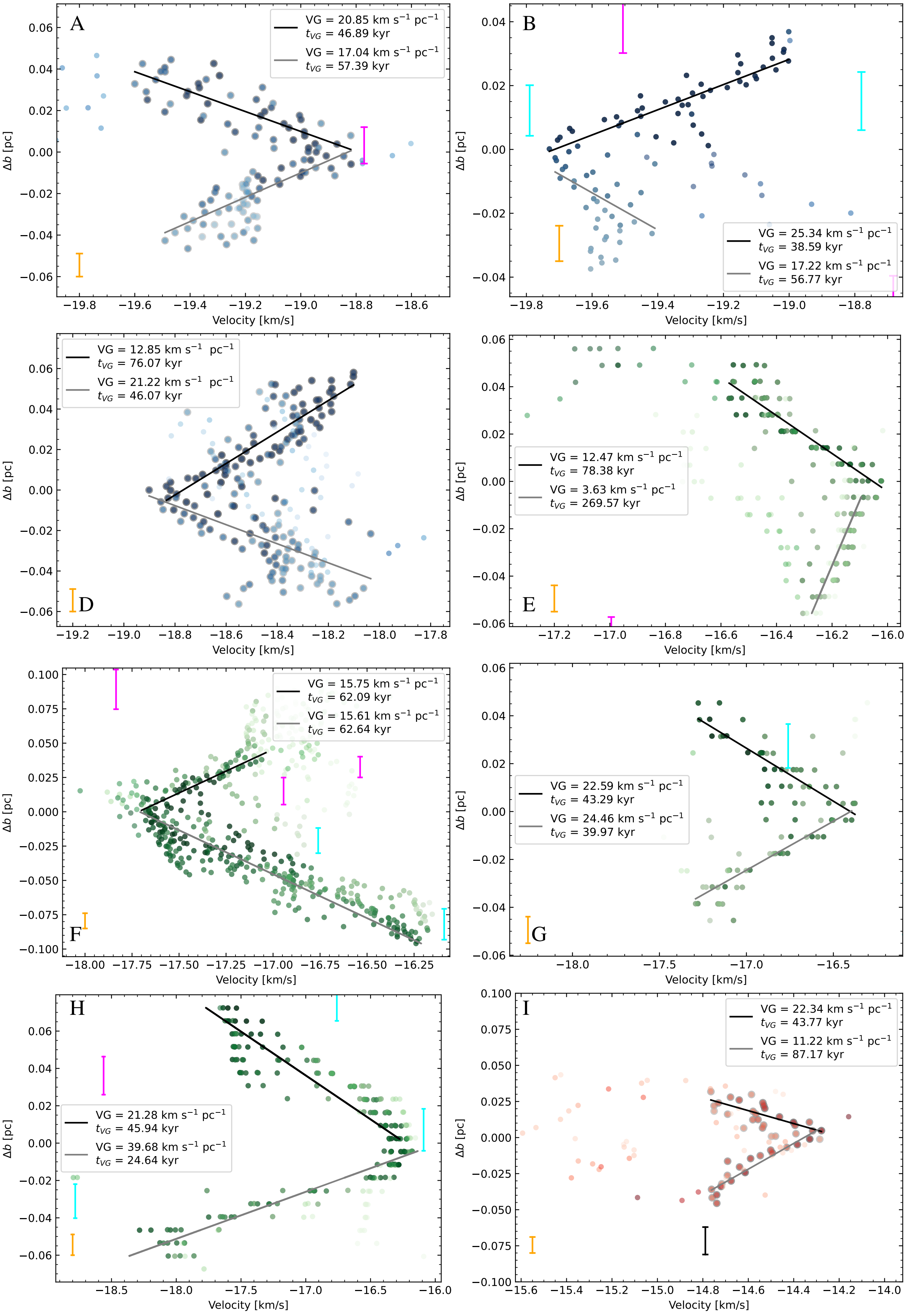

Fig. D.2: V-shaped structures listed in Table D.1, with the exception of "C" shown in Fig. 10. We indicate the "V-shape ID" from Table D.1 at the top/bottom left corner of each plot. The colors of the distributions, DCN and DCN & N_2H^+ derived core velocities, and beam size follow the same color and marker convention from Fig. 9. See Appendix D for clarifications regarding projection effects on these diagrams.

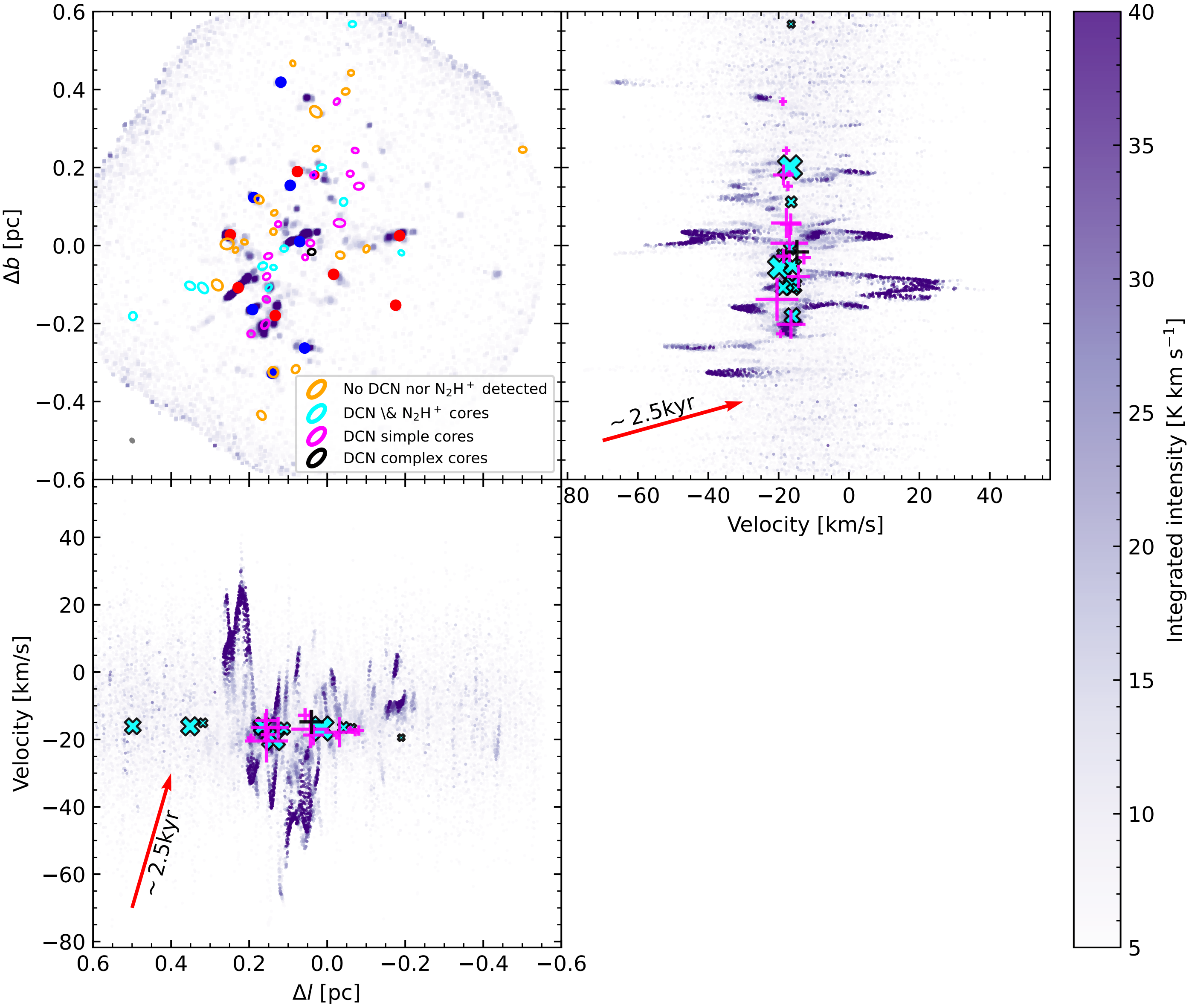

Fig. E.1: ALMA-IMF 12 m SiO equivalent of Fig. 9 using data from Cunningham et al. (2023). For the cores, we use the same marker and color convention from Fig. 9. With filled blue, red, and 'red+blue' circles we represent the SiO outflow candidates (Towner et al. 2024). With red arrows we indicate a VG = 400 km s^{-1} pc^{-1} corresponding to a timescale t_{VG} = 2.5 kyr. The velocity range (ΔV) covered by the SiO emission is ~80 km s^{-1}, about 10 times the velocity range traced by N$_2$H$^+$. This velocity difference suggests that SiO is tracing processes (outflows) ~ 100 times more energetic (e_k = ΔV/2) than N$_2$H$^+$ (possibly infall).